INDUCING DIFFUSE PHASE TRANSITIONS IN BARIUM TITANATE USING Ga^{3+}-Ta^{5+} DIPOLE PAIR SUBSTITUENTS

BY

VIGNASWARAN KALIYAPERUMAL VEERAPANDIYAN

A THESIS

SUBMITTED TO THE FACULTY OF

ALFRED UNIVERSITY

IN PARTIAL FULFILLMENT OF THE REQUIREMENTS
FOR THE DEGREE OF

MASTER OF SCIENCE

IN

CERAMIC ENGINEERING

ALFRED, NEW YORK

JUNE, 2017

INDUCING DIFFUSE PHASE TRANSITIONS IN BARIUM TITANATE USING Ga^{3+}-Ta^{5+} DIPOLE PAIR SUBSTITUENTS

BY

VIGNASWARAN KALIYAPERUMAL VEERAPANDIYAN

B.Tech. ANNA UNIVERSITY (2015)

SIGNATURE OF AUTHOR_____

APPROVED BY_____

STEVEN C. TIDROW, ADVISOR

_____

WALTER A. SCHULZE, ADVISORY COMMITTEE

_____

STEVEN M. PILGRIM, ADVISORY COMMITTEE

_____

SCOTT T. MISTURE, ADVISORY COMMITTEE

_____

CHAIR, ORAL THESIS DEFENSE

ACCEPTED BY _____

ALASTAIR N. CORMACK, INTERIM DEAN
KAZUO INAMORI SCHOOL OF ENGINEERING

ACKNOWLEDGMENTS

I would first like to thank my advisor Dr. Steven Tidrow, Inamori Professor, New York State College of Ceramics at Alfred University for all the wonderful discussions we had over the past two years. I sincerely thank him for all the freedom he gave me to pick my own research direction, to travel around the United States for several technical conferences and helping me to take the right direction both in my research and my career. I would like to thank my research committee members Dr. Walter Schulze, Dr. Steven Pilgrim and Dr. Scott Misture for their constant help and guidance towards my successful completion of the degree. I would like to extend my special gratitude to Dr. Walter Schulze for all the time he invested on me to teach various aspects of ferroelectricity. I would like to thank my colleague Taylor Perry and technical staff members Mr. Tom Steere, Mr. Francis Williams, Mr. Gerald Wynick, Mr. James Thiebaud and Mr. Swavek Zdzieszynski for helping me with my research. I would like to thank my mentors Dr. Omprakash Chakrabarti, Senior Principal Scientist, Central Glass and Ceramic Research Institute, India, and Dr. Thenmuhil Deivarajan, Assistant Professor, Department of Ceramic Technology, Anna University, India for constantly encouraging me to pursue graduate education in ceramics, abroad.

My sincere gratitude to my friends Nick, David, Sarah, Peter, Aubrey, Kiel, Alec and Andrew for all your time in trying to help me understand the American culture and being supportive for the past two years. Also, special thanks to Yuri, Sahar and all the other wonderful people I am leaving behind in Alfred, for your time and support. Last but not the least I would like to thank my mom, dad and my sister who are the pillars of support all my life. This accomplishment would not have been possible without them.

TABLE OF CONTENTS

Page

LIST OF TABLES

LIST OF FIGURES

ABSTRACT

$Ba\{[Ga_x,Ta_x]Ti_{(1-2x)}\}O_3$ with x equal to 0, 0.0025, 0.005, 0.01, 0.025 and 0.05 have been prepared by conventional solid-state reaction and sintered to greater than 95% density. Structural and dielectric characterization have been performed to investigate the effect of dipole-pair concentration on the properties. Dielectrically, the $Ba\{[Ga_x,Ta_x]Ti_{(1-2x)}\}O_3$ phase transition evolves from a classic ferroelectric to a diffuse phase transition (DPTs) as x increases. $Ba\{[Ga_x,Ta_x]Ti_{(1-2x)}\}O_3$ for $x \geq 0.01$ possesses diffuseness parameters comparable to $Pb(Mg_{1/3}Nb_{2/3})O_3$-$PbTiO_3$ (PMN-PT), yet it lacks the frequency and temperature dependence of T_m necessary to be a strictly defined relaxor ferroelectric. Additionally, $Ba\{[Ga_{0.05}, Ta_{0.05}]Ti_{0.9}\}O_3$ possesses a relative permittivity, ε_r, of 700±16% and dissipation factor less than 0.05 at 10 kHz within the temperature range [-75°C, 120°C]. In comparison to $BaTiO_3$, $Ba\{[Ga_x,Ta_x]Ti_{(1-2x)}\}O_3$ possesses enhanced electrical resistivity and greater time constant at and above room temperature. Through varying the concentration of dipole-like substitutions, material evolution of properties could be systematically investigated and material properties like resistivity, RC time constant, breakdown strength, maximum ε_r, temperature sensitivity of ε_r, dissipation factor, etc. can be individually optimized or any combination(s) of material properties can be optimized to achieve desired device or system performance. The relaxation of ε_r is found to increase linearly with the dipole concentration. *In-situ* XRD, including Rietveld refinement, have been performed to determine the lattice parameter, coefficient of thermal expansion and phase transition temperature of each composition within the temperature range [RT, 1000°C]. The unusual properties of $Ba\{[Ga_x,Ta_x]Ti_{(1-2x)}\}O_3$ are discussed in context with available models describing donor and acceptor dopants spatially separated in the parent matrix that inter-relate lattice parameter, Curie temperature, and other material properties.

INTRODUCTION

A. Perovskite structure:

Perovskite is the classification name given to materials based on the general crystal structure and bonding arrangement of the mineral calcium titanate ($CaTiO_3$). After discovery of the mineral $CaTiO_3$ in the Ural Mountains of Russia by Gustave Rose in 1839, the mineral was named perovskite in recognition of the Russian mineralogist Lev Perovski (1792 – 1856)[1]. At room temperature $CaTiO_3$ has the crystal structure orthorhombic *Pbnm* and undergoes reversible phase transformation to tetragonal *I4/mcm* at 1512 K. It transforms to ideal cubic $Pm\bar{3}m$ at a temperature of 1636 K and remains $Pm\bar{3}m$ cubic until its melting temperature of 2248 K[2]. In the ideal cubic perovskite structure, $Pm\bar{3}m$, atoms have a face centered arrangement and the structure is cubic close-packed with larger A-site (A) cations and C-site (C) anion forming the FCC lattice with the smaller B-site (B) cation possessing octahedral coordination with anions. The bonding environment is schematically represented in Figure 1. In the perovskite structure, the co-ordination number of A cation is twelve and the B cation and C anion coordination numbers are each six[3].

Although, perovskites possess the general chemical formula ABC_3, which is often written, ABX_3, perovskites possess significant variation of chemical formula to account for excess or deficient amounts of the anion, C. For instance, $SrMnO_3$ and $LaMnO_3$, anion deficient and anion excess compositions are described using the general formula $ABC_{3-\delta}$ and $ABC_{3+\delta}$, respectively. For cation ordering, the perovskite can be described using the formula, $A_2B'B''C_6$, with the ordered or double perovskite structure ideally cubic $Fm\bar{3}m$. Perovskites and ordered perovskites may exhibit a wide range of crystal structures as discussed by A.M. Glazer[4] and C.J. Howard[5], respectively. There are many addition chemical variations of the perovskite not covered here which describe layered perovskites as well as a wide range of other perovskites[6]. Many of these perovskites yield a ferroelectric response.

Ferroelectrics are a special classification of functional materials that have significant economic impact. Although ferroelectrics and relaxor ferroelectrics are not

limited to perovskite materials, a significant number of technologically valuable materials are found within perovskites. For example, lead titanate, strontium titanate, lead zirconate titanate and solid solutions of lead titanate and lead zirconate titanate[7,8] which are all perovskites, are highly studied ferroelectric and relaxor ferroelectric materials used commercially.

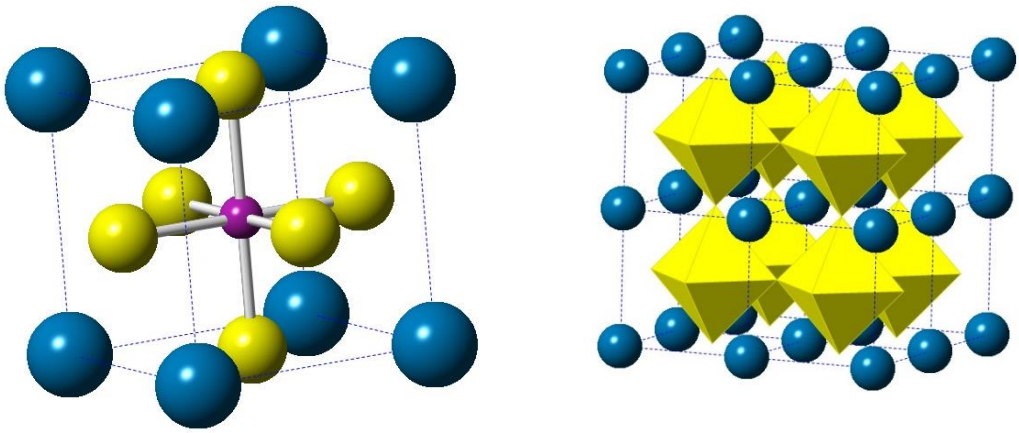

Figure 1. The ideal cubic perovskite structure (left) and the bonding environment of ideal perovskite structure (right).

For ferroelectrics and related materials, the perovskite structure can tolerate a wide range of substitutions or dopants in the A and B site which can result in significant variation of material properties[9,10] because the dopants or substitutions can change the polarization energy per unit volume, band structure, etc. The theoretical packing density of the close packed perovskite structure can range from 0.52 to 0.76 and can be increased further by selective elemental substitution. The lattice sites may incorporate multiple ions that lead to complex perovskites like $PbMg_{1/3}Nb_{2/3}O_3$ (PMN), $NaBiTiO_3$ etc[11,12]. As a result, a perovskite can take on a wide range of crystal structures depending upon the nature of atoms incorporated, energy states, with the material rarely forming the ideal cubic perovskite structure. The non-cubic or non-ideal perovskite structure typically transform into the ideal cubic perovskite structure at elevated temperature[13].

Perovskite materials are often structurally analyzed using a semi-empirical relationship known as Goldschmidt tolerance factor (GTF)[14], which can be expressed as:

$$T = \frac{R_A + R_C}{\sqrt{2}(R_B + R_C)} \quad (1)$$

where R_A, R_B and R_C are the ionic radii of the A, B, and C-site atom(s), respectively. In Goldschmidt's formalism, T ranges from about 0.77 to about 1.05 with the "ideal" cubic perovskite forming when T is about 1.00. For $T > 1$, the material is often associated with high permittivity material properties, which include ferroelectric materials. For $T < 1$, the material is often associated with low symmetry materials[15]. GTF, as a relatively simple tool, has been utilized by the scientific community for nearly a century to guide discovery and development of new perovskite materials. The room temperature radii of R.D. Shannon[16] have been utilized within GTF to estimate the structure, lattice parameter and volume of a wide range of perovskites. Unfortunately, the GTF correlation relation has over time become less effective as a tool for guiding research due to the growing number of inconsistencies that the model has provided in *a priori* prediction of crystal structure, cubic or non-cubic, as well as lattice parameter or volume[17]. Some of these GTF inconsistencies are attributable to ionic radii refined at room temperature which are reported based on correlations of both cubic and non-cubic materials which include significantly differing crystal habits. In addition, the limitations of room temperature or temperature static radii data sets significantly degrade the ability of GTF to *a priori* model the dynamic evolution of the crystal structure, lattice parameters and volume over temperature ranges of interest for device operation. Therefore, new temperature dependent models such as the "new simple material model" (NSMM)[17] are under investigation that can provide material properties beforehand with high fidelity thereby reducing the search space and time to develop new material systems that address specific device and system requirements.

NSMM is a coordination dependent hard sphere ionic radii model that incorporates five planar constraints and minimum and maximum packing densities while GTF considers only two principal directions in defining lattice parameter[18]. NSMM calculations are slightly more complicated as compared to GTF but NSMM demonstrates

significant improvement in predicting the lattice parameter, volume, and structure at room temperature and provide temperature evolution of material properties. Determination of temperature dependent dielectric properties, polarization induced structural phase transition and determination of Curie constant have been demonstrated by incorporating the Clausius-Mossotti relation within NSMM[19]. NSMM appears to provide a road map relating fundamental ion properties, radii and polarizability, with temperature dependent packing density, lattice parameter, volume, permittivity, and both polarization and volume induced phase transitions. Understanding the basic parameters such as temperature dependent polarizability and ionic radii can be used by researchers to relate them to more complicated material properties such as temperature dependent crystal structure and phase transformations, temperature dependent relative permittivity (ε_r), band gap etc. Thus, NSMM may be a useful tool for an experimentalist in the search of new materials to meet specific requirements.

B. Dielectrics and insulators

Dielectrics and insulators are materials with high electrical resistivity, typically greater than 10^8 Ω·m and can be used to store electrical energy through effects of polarization resulting in the formation of dipoles. When the dielectric is placed in an electric field, there is no long-range flow of charge; however, atoms locally react to oppose the electric field by polarizing or setting up a dipole moment that opposes the external applied electric field. In other words, under the effect of an electric field, the positive nuclear core shifts in the direction along the electric filed while the negative electron cloud shifts in the opposite direction. The temperature dependent volume and energy states of atoms comprising the material, as manifested through radii and polarizability, determine the material's relative permittivity, which is often inappropriately misnamed dielectric constant. The functional interrelationship among permittivity and ion properties has recently been demonstrated and is given by the fundamental Clausius-Mossotti relationship which is discussed later within this same section.

As discussed, the material's relative permittivity, which is often loosely called "dielectric constant", is a function of the temperature dependent volume and energy

states, radii and polarizability, of the atoms comprising the material. An individual atom or ion in a dielectric is not subjected directly to the applied electric field ($\boldsymbol{E_a}$) but rather to a local field which is less than or equal to $\boldsymbol{E_a}$ as shown in Figure 2. Macroscopically, the properties of any dielectric material are the result of complicated and complex electric field interactions among local ions which give rise to the local fields which collectively interact to establish the long-range order of interactions. Lorentz calculated the local field $\boldsymbol{E_L}$ using a spherical region selected within the dielectric[20]. The region outside the sphere can be viewed as a continuum while inside the sphere, the local interactions give rise to the discontinuous nature of dielectrics. In the real case, the macroscopic field ($\boldsymbol{E_m}$) and the local field $\boldsymbol{E_L}$ relationships can be written as,

$$\boldsymbol{E_m} = \boldsymbol{E_a} - \boldsymbol{E_{dp}} \tag{2}$$

$$\boldsymbol{E_L} = \boldsymbol{E_m} + \boldsymbol{E_p} + \boldsymbol{E_d} \tag{3}$$

where, $\boldsymbol{E_{dp}}$ is the depolarization field; $\boldsymbol{E_p}$ is the contribution from the charges at the surface of the spherical region under consideration; $\boldsymbol{E_d}$ is the contribution due to dipoles within the boundary; and other symbols are as previously defined.

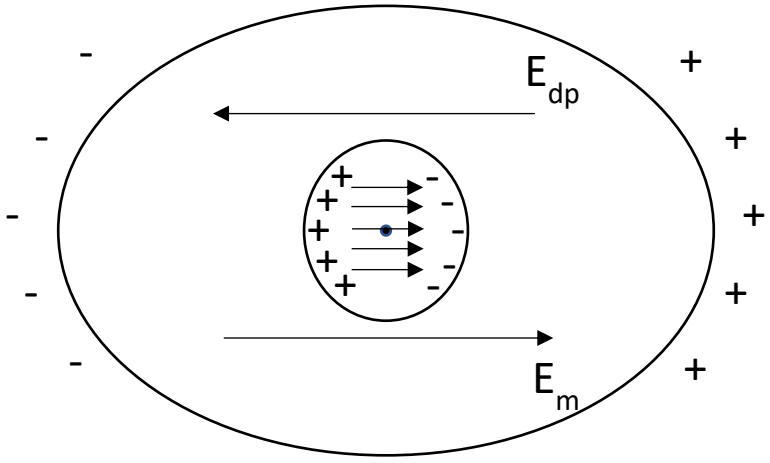

Figure 2. The local field in a dielectric material.

For particular crystals of higher symmetry (isotropic materials), $\boldsymbol{E_d}$ = 0 and $\boldsymbol{E_L}$ can be written as,

$$\boldsymbol{E_L} = \boldsymbol{E_m} + \frac{P}{3\varepsilon_o} \tag{4}$$

The dipole moment *p* induced in the area of interest can be written as,

$$p = \alpha \boldsymbol{E_L} \tag{5}$$

where α is the polarizability within the area of interest or the dipole moment induced per unit local field. The total dipole moment, *P*, in the area of interest possessing density *N* of dipole moments, p, is given by,

$$P = Np = N\alpha(\boldsymbol{E_m} + \frac{P}{3\varepsilon_o}) \tag{6}$$

Rearrangement of (6) leads to the Clausius-Mossotti relationship[21],

$$\frac{\varepsilon_r - 1}{\varepsilon_r + 2} = \frac{N\alpha}{3\varepsilon_o} \tag{7}$$

where ε_r is the relative permittivity, and ε_o is the permittivity of free space, with other symbols previously defined.

R. D. Shannon[22] calculated the polarizabilities per unit volume through rewriting equation (7) in terms of a dimensionless quantity, ε_r,

$$\varepsilon_r = \frac{3V_m + 8\pi\alpha_T}{3V_m - 4\pi\alpha_T} \tag{8}$$

where α_T is the total polarizability within the molar volume, V_m.

When alternating electric fields, including electromagnetic radiation, interact with a dielectric, the atoms comprising the dielectric material impede the propagation of the wave as compared to propagation in vacuum. To appropriately describe such interactions, the permittivity of the material, a complex quantity, ε^*, is mapped into the complex plane as described through the equation:

$$\frac{\varepsilon^*}{\varepsilon_0} = \varepsilon_r^* = \varepsilon' + i\varepsilon'' \tag{9}$$

where the complex relative permittivity, ε_r^*, is the superposition of ε' the real in phase and ε'' the imaginary out of phase component, respectively.

The real component is related to the energy storage and the imaginary component is related to the energy loss of the material. Specifically, the energy loss within the dielectric or dielectric loss is expressed as:

$$\tan \delta = \frac{\varepsilon''}{\varepsilon'} \tag{10}$$

where tan δ is named the loss tangent of the material with other symbols previously defined.

There are four mechanisms[23] generally considered responsible for the field induced polarization that are active or dominate in a specific frequency range as shown in Figure 3. The four mechanisms are (i) space charge polarization, (ii) dipolar polarization, (iii) ionic polarization and (iv) atomic polarization. For dielectric measurements discussed in this thesis, measurements are between 100 Hz to 1 MHz. In the low frequency range, ≤ 10^4 Hz, each of the mechanisms can track with the electric-field; and the measured values of relative permittivity are a superposition of each of the four mechanisms. The maximum frequency for which a polarization effect can track with the frequency can be estimated using the lightest particle, the mass of the electron. By equating the classical kinetic energy of the particle to the quantum mechanical energy related to frequency and by setting the maximum velocity of the particle to the speed of light, the maximum frequency may be estimated as:

$$f_{max} < \frac{mc^2}{2h} \tag{11}$$

where *m* is the mass of the particle, c, the maximum velocity, is the speed of light and *h* is Plank's constant. For an electron, $f_{max} \approx (10^{18} - 10^{19})$Hz. For ions, where masses are in excess of 10^3 that of the electron, the cut-off frequency is less than 10^{15} to 10^{16} Hz. Thus, due to the inertial mass or equivalent associated with the mechanism, each mechanism possesses an upper cut-off frequency above which the mechanism is no longer able to track with the time dependent electric or electromagnetic field.

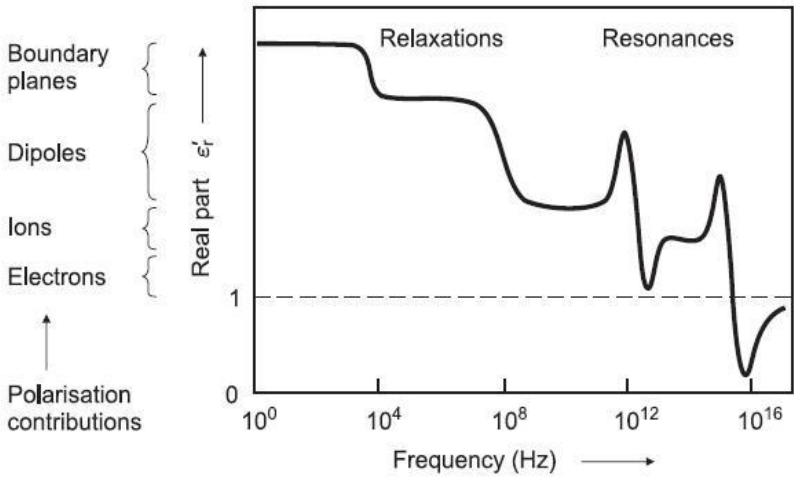

Figure 3. Frequency dependent polarization mechanisms[24].

C. Ferroelectricity:

Although ferroelectricity was first discovered in Rochelle Salt in 1920, barium titanate (BT) is the first ceramic material in which ferroelectric behavior was observed and is presently the most widely used high permittivity ceramic material[25]. BT was first discovered, nearly simultaneously in the United States by Wainer and Salomon in 1942, Russia by Vul in 1944 and Japan by Ogawa in 1944[26]. At that time mica was the most used capacitor material; however, the supply of mica to the United States from South America was hindered during World War II. Due to the pressing wartime need for improved materials and devices, research was accelerated in the area of alternative high permittivity materials for capacitor technology to improve the performance and reduce the weight and/or size of electronics. The discovery of $BaTiO_3$ was of importance due to the high relative permittivity for reducing the size and weight of devices through increasing capacitance per unit volume. It was not until 1947 that the piezoelectric properties of $BaTiO_3$ were reported by Gray at Erie Resistor using electrically poled $BaTiO_3$[27]. The dielectric anomaly in ceramic BaO-TiO_2 was first explained by Von Hippel (USA)[28] and subsequently refined by many authors. The discovery of ferroelectric switching in these ceramics is extremely important since it had been believed until that time that ferroelectricity was associated with hydrogen bonding.

The crystal structure of $BaTiO_3$ in the ferroelectric phase was first reported by Helen D. Megaw[29] followed by Kay and Vousden[30] who documented a series of ferroelectric-ferroelectric phase transitions before the material enters the paraelectric region. The Curie point (T_c ~ 131°C for $BaTiO_3$ as reported in the present work) is the temperature at which the tetragonal to cubic phase transformation occurs on heating. $BaTiO_3$ possesses other phase transformations: orthorhombic to tetragonal (O-T) at ~20°C; and, rhombohedral to orthorhombic (R-O) at -70°C, which are often designated T_{c_2} and T_{c_3}, respectively. Below T_c, $BaTiO_3$ is distorted to a tetragonal structure with the polar axis along the *c*-direction. For orthorhombic and rhombohedral $BaTiO_3$ structures, the polar axis is along the face and body diagonal of the prototypic cubic phase, respectively. Above T_c, the temperature dependent ε_r follows the Curie-Weiss law:

$$\varepsilon' \sim \frac{C}{T - T_c} \tag{12}$$

where, C is the Curie constant.

The temperature dependent phase transformations and the corresponding change in the ε_r of $BaTiO_3$ are shown in Figure 4.

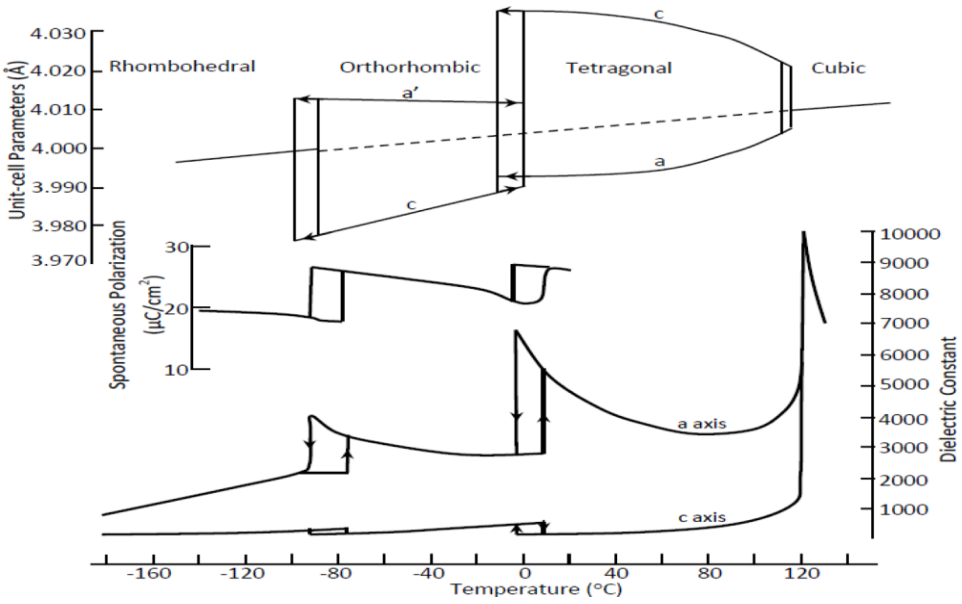

Figure 4. Temperature dependent phase transformation and the corresponding change of ε_r for $BaTiO_3$[31].

Above the Curie temperature, the material is in the cubic phase and is paraelectric. As the temperature is lowered to or just below the Curie temperature, the material undergoes a transition to the tetragonal phase through spontaneous polarization. In tetragonal $BaTiO_3$, the Ti^{4+} ion sits along the *c* axis within four of eight degenerate energy wells[32]. Reversal of polarity takes place with the application of a sufficiently large electric field in the direction opposite to the polarization and forces the Ti^{4+} ion to pass through the energy barrier (the 001 plane) and into the other set of degenerate wells. Spontaneous polarization within the ferroelectric material is not uniformly aligned and the areas with the spontaneous polarization aligned along the same direction are called ferroelectric domains. The boundary between domains is called a domain wall. These domains can be reoriented to form a polar material by the application of sufficiently intense static field along a specific direction sometimes at elevated temperature. This process of alignment is called "poling"[33].

One of the defining features of a ferroelectric material is the hysteresis loop as shown in Figure 5, where polarization is measured as a function of AC electric field. Hysteresis is a result of domain wall switching. In general, the overall polarization of the ferroelectric crystal will be zero because of the equal number of domains oriented in random directions. When a small field $\boldsymbol{E}$ is applied, the material behaves like a normal dielectric since the $\boldsymbol{E}$ is not strong enough to overcome the potential energy barrier, the O-A segment of Figure 5. As $\boldsymbol{E}$ increases, the cations obtain sufficient energy to overcome the energy barrier and will be able to jump from one random well position to another well position most closely aligned with the field which results in switching of domains, the segment A-B of Figure 5. At strong enough $\boldsymbol{E}$, switching will result in a single domain saturation state, segment B-C in Figure 5. On reducing and reversing $\boldsymbol{E}$, the converse process takes place, but traces along a new path consistent with creation of create new domains in the opposite direction. The polarization exhibited at zero field is called remnant polarization (P_r). Extrapolation of linear segment B-C in the P-E loop to the *y*-axis is defined as the spontaneous polarization (P_s) for a fully poled crystal. The applied electric field that can switch the domains of the ferroelectric material back and forth is the coercive field (E_c). Once poled, the material continues to follow the hysteresis loop and will not return to zero net polarization at $\boldsymbol{E} = 0$ until the material is raised above

T_c or otherwise depoled where it will lose polarization, become cubic, and possess paraelectric properties.

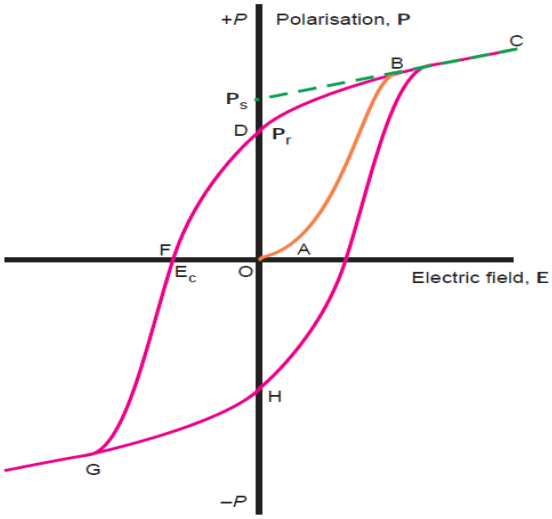

Figure 5. Hysteresis behavior of the polarization versus the applied electric field of a ferroelectric material[34].

D. Relaxor ferroelectrics:

A normal ferroelectric has a high ε_r peak value in the temperature dependent ε_r response at the structural phase transition with full width half maximum (FWHM) of the peak being narrow as a function of temperature, typically less than 20 K wide. In numerous complex ferroelectric perovskite solid solutions, the dielectric response differs from normal ferroelectrics[35]. One such characteristic is a diffuse phase transition (DPT) where the FWHM of the permittivity peak can be significantly greater than 20 K. Such materials with peculiarities in their ferroelectric behavior are grouped within a special class of ferroelectrics called relaxor ferroelectrics, with the term often shortened to "relaxors". Figure 6 is the typical dielectric response of the widely studied lead based relaxor material-PMN.

Relaxor ferroelectrics are considered as an electric analog of magnetic spin glasses since they are all characterized by spin glass freezing of the nano-domains[36]. The

relaxors are extremely useful materials for practical applications such as multilayer capacitors (MLCs), microwave (MW) tunable devices etc., while the practical applications for magnetic spin glasses are yet to be identified. One main feature of a ferroelectric relaxor material is the quenched compositional disorder of A and/or B cations resulting in what is termed frustrated ferroelectrics. There are at least three distinguishing properties of relaxors:

- within the dielectric response, the weak field ε_r reaches a very high value even up to 20000 near T_m, the temperature at which ε_r is maximum, yet, T_m does not mark a macroscopic phase change and T_m increases with the frequency resulting in dielectric dispersion. In most of the relaxor ferroelectrics $T_c < T_m$, where T_c is the temperature at which the relaxor material or disordered perovskite undergoes transformation from ferroelectric to ergodic relaxor sate before entering the paraelectric state[36].
- spontaneous polarization of the hysteresis response is not suddenly lost at T_m but instead gradually decays to zero; and,
- x-ray diffraction data indicate no evidence of a macroscopic phase change near T_m.

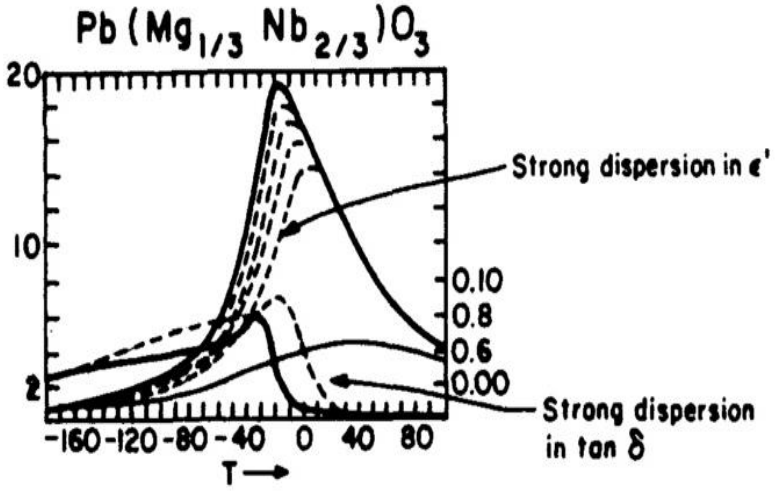

Figure 6. The typical dielectric response of the widely studied lead based relaxor material (PMN)[37].

The first explanation of $PbMg_{1/3}Nb_{2/3}O_3$ (PMN) relaxors was given by G.A.Smolenski, in which the Mg and Nb ions do not order thus resulting in fluctuations in Mg:Nb concentration. Such disorder results in an intimate mixture of ferroelectric and para-electric regions which become completely polar as the temperature is reduced. In another facet of this approach, the stability of small polar micro regions explains the phenomenon[38].

Using Devonshire's formalism[39], the free energy as a function of polarization for polar regions can be schematically illustrated as shown in Figure 7. Macroscopic domain states are stable since the energy separating the alternative domain states are many factors greater than kT. Within a polar nano domain, the energy barrier is reduced to close to kT making the local region unstable through thermal agitation[37]. Thus, when structurally characterized with x-ray diffraction these materials exhibit cubic symmetry with unusual peak broadening and yet possess net polarization properties. Such materials are grouped under pseudo-cubic symmetry; that is, the material system by x-ray diffraction technique is characterized to possess cubic symmetry yet, the material is not strictly cubic. The cation distribution in the B site of PMN has been depicted in either of two cases to support or deny Smolenski's explanation on cation distribution in relaxors as follows,

Case 1: One distribution scheme, as developed through tossing a coin and recording the heads and tails in the lattice, results in significant local heterogeneities or segregation of dopants.

Case 2: Another distribution scheme provides uniform composition or homogeneity, and results in translational symmetry being completely recovered down to the unit cell scale.

If the Smolenski's hypothesis is correct, diffuse or relaxor behavior is expected in Case 1 while a ferroelectric phase transition will exist in Case 2 because of the fully ordered state. The order disorder behavior has been studied in detail by C. Randall et al. by annealing and quenching of $Pb(Sc_{1/2}Ta_{1/2})O_3$ samples to obtain ordered and disordered cation distributions, respectively[40].

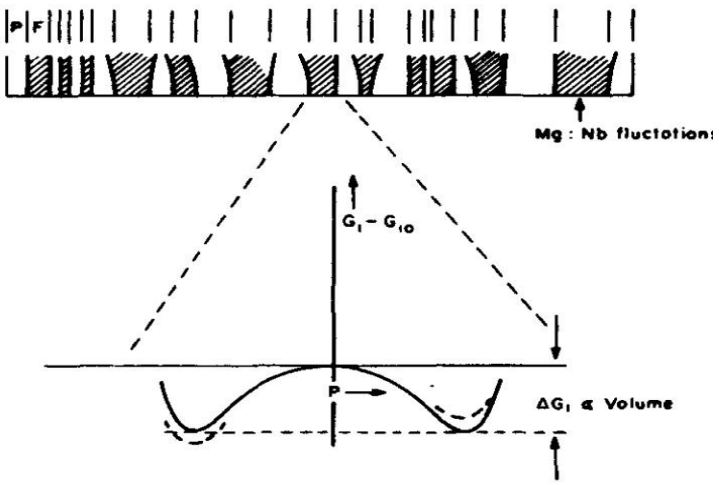

Figure 7. Gibbs free energy in the polar micro region[37].

A ferroelectric material with a diffuse phase transition (DPT) is characterized by broadening of the ε_r response as a function of temperature. The important characteristics of relaxors are: (i) a relatively large separation in temperature between the ε_r maximum and dielectric loss maximum; and, (ii) deviation from the Curie-Weiss law within the paraelectric region[35] which is usually above T_m, where T_m is the temperature at which the ε_r is maximum. A DPT by definition can be different from strict-relaxors by: (i) possessing Curie-Weiss law behavior in the paraelectric region; and, (ii) undergoing a macroscopic phase transition near T_m. Relaxors and DPT have been studied by developing various models to describe the dielectric anomaly such as deviation from Curie-Weiss law and diffuseness in phase transition. The parameter ΔT_m is used to describe the degree of deviation from the Curie-Weiss law through the relation:

$$\Delta T_m = T_{cw} - T_m \tag{13}$$

where T_{cw} is the temperature at which the permittivity starts to deviate from the Curie-Weiss law and other terms are previously defined.

Smolenski and Rokov attempted to describe the broad transition peak by a diffuseness parameter[41] using the expression:

$$\varepsilon_m = \varepsilon \, exp \frac{(T - T_c)^2}{2\delta^2} \tag{14}$$

where, δ is the diffuseness parameter which quantifies the width of the diffuse phase transition; ε_m is the maximum ε_r value and other terms as defined previously.

While equation (14) is widely used to quantify the diffuse phase transition, the equation is believed to be valid only for $\delta >> T - T_c$ and is not in good agreement for many relaxor materials. The diffuseness of phase transitions of ferroelectrics exhibits differing degrees of diffuseness ranging from a ferroelectric like phase transition, which follows a Curie-Weiss relation in the paraelectric regime to DPT's including relaxor behavior, which are typically fit using the modified Curie-Weiss relation. The modified Curie-Weiss law or the power law has been proposed to describe the diffuseness of a phase transition ranging from a normal ferroelectric to a complete DPT through the equation:

$$\frac{1}{\varepsilon} - \frac{1}{\varepsilon_m} = \frac{(T - T_m)^\gamma}{C'} \tag{15}$$

where C' is the Curie-Weiss constant; γ is the diffuseness parameter and other terms have previously been defined.

The diffuseness parameter γ gives information on the type of phase transition with γ varying from 1, a normal ferroelectric, to 2 for a complete DPT. The parameter, γ, can be directly obtained from the slope of line in a $\ln(1/\varepsilon - 1/\varepsilon_m)$ versus $\ln(T - T_m)$ plot.

Pilgrim et al. summarized several attempts made by researchers to model the diffuse phase transition that are inconsistent in calculating the diffuseness parameter but yet are widely accepted and utilized by the research community. Most of the discussed models are valid above T_m yet fail to explain the dielectric dispersion in relaxors below T_m. The summary used several available models to calculate the diffuseness parameter and demonstrated the significant deviations in the calculated values. Pilgrim et al. concluded that variations of diffuseness parameter can be minimized through: (i) appropriate selection of the temperature range for each particular set of frequency data being used within the power law equations so that the diffuseness parameter does not become a significant function of the maximum temperature of measurement; and, (ii)

utilizing enough data points (> 50) to reduce statistical uncertainties[41] with the linear correlation fit defining the diffuseness parameter.

E. High permittivity ceramics

Dielectrics with ε_r exceeding 1000 are primarily ferroelectric materials and are more sensitive to temperature, field strength and frequency compared to low permittivity ceramics[42,43]. There have been numerous attempts by material scientists around the world to improve the temperature stability of these high permittivity materials[44,45]. A wide range of properties in $BaTiO_3$ is made possible by careful doping or substituting for Ba or Ti. The ε_r of "pure" $BaTiO_3$ varies with many factors such as purity of the raw material, grain size of the polycrystalline material[46], density, method of preparation[47] etc. Understanding the domain wall motion is important because of its significant contribution to the dissipation factor. Being a co-operative phenomenon, it is challenging to completely control perovskite material dielectric properties. The Curie temperature can be systematically controlled for a specific application of the material by careful addition of substituent elements at the A site with the atomic radii ranging between 130 and 160 pm. Isovalent substitution is more common when compared to aliovalent substitution because of solubility limits. Boththe dielectric properties of the material will change by introducing specific ions as will electrical properties like resistivity, time constant, breakdown voltage and the band gap.

F. Random charge compensated dipole pairs:

The electrical characteristics such as conductivity, ε_r, optical birefringence etc., of perovskite ferroelectric materials can easily be tailored by introducing specific elements in the host material in the form of dopants or substituents. Doping and substituents are fundamentally two different methods that have been used to tailor the electrical properties of materials including $BaTiO_3$. Substitution generally refers to isovalent replacement, where an atom in the crystal structure is replaced with a substituent atom of the same valence state. Doping generally refers to aliovalent substitution in which the atom in the crystal structure is replaced with an atom of a different valence state. A and B-site substituents, i.e., aliovalent, typically result in a shift in T_c of the material, to higher or

lower temperature depending upon the substituent and amount. The sharpness in the peak of the ε_r typically is unaffected by the substitution although a significant change may occur for both the peak permittivity and electric field tunability (ability to tune the ε_r response by varying applied electric field) of the material.

Dipole-like substitution refers to replacing the same atom in two adjacent or nearly adjacent unit cells with charge compensated pairs, one dopant of higher and the other dopant of lower charge, to preserve charge neutrality within the local region of the two unit cells as illustrated in Figure 8. Conceptually, while regionally the material remains charge neutral, a permanent dipole is created in the region with the dipole strength depending upon the charge difference and separation distance of the two doped unit cells. Although these fields will vary in direction and magnitude, they will superimpose with each other and may become quite large[48]. Specifically, dipole-like substituted $BaTiO_3$ has been compared with $Ba(Ti_{0.70}Zr_{0.30})O_3$ to assess the viability of using $BaTiO_3$ based relaxors for tunable microwave applications. $BaTi_{0.90}Ga_{0.05}Nb_{0.05}O_3$ shows electric field tunability comparable to BT but has increased loss at microwave frequencies. The origin of the increased loss for such relaxor materials is unclear and it is in general considered to be dipole flipping in the form of nano clusters[49]. $Ba(Y_{0.05}, Sb_{0.05})Ti_{0.90}O_3$ shows a diffuse phase transition with the T_c being raised to ~200°C and exhibits no characteristic of a relaxor[50].

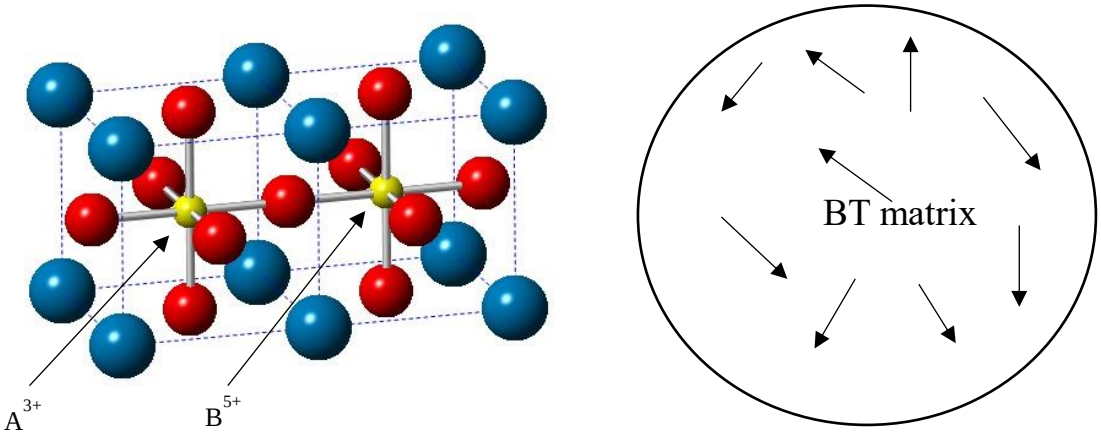

Figure 8. Schematic of a random charge compensated dipole pair from two unit cells of BT (left) and illustration of random dipoles in the BT matrix (right)

G. Objectives

Conceptually, relaxor ferroelectrics and DPT materials possess separable characteristics which are often misunderstood and misreported. One structural characteristic of relaxors is the compositional disorder which is static at all relevant temperatures. The work here primarily focuses on DPT materials in which DPT is induced by random electric field interactions from dipole pairs (DP). The DP in the form of donor and acceptor dopants separated spatially by short nanoscale distances introduces a random electric field interaction in the parent matrix which results in DPT.

The main objective of this work is to distinguish or contrast the properties of relaxors from DPT materials by introducing the random electric field interaction in the form of dipoles randomly distributed while maintaining the compositional order; thereby, maintaining the long-range ferroelectric nature of the parent material. Thus, the main objectives of the present work are to:

1. systematically study the solubility limit of the DP-(Ga,Ta) in a $BaTiO_3$ parent matrix;
2. understand the effects on dielectric properties of DP-(Ga,Ta) in the $BaTiO_3$ parent matrix;
3. study the effect of DP-(Ga,Ta) on the electrical resistivity, activation energy and time constant;
4. study the slow evolution of sharp ferroelectric phase transition to DPT and the dielectric relaxation with increasing DP concentration; and,
5. study the oxidation states of B site donor/acceptors and Ti to confirm or refute the consistency with the hypothesis of charge compensated dipole-like dopant-substitutions which introduce random electric field interactions.

MATERIAL FABRICATION

A. Batching

Batches of 50 g of $Ba\{[Ga_x,Ta_x]Ti_{(1-2x)}\}O_3$ (BGT*x*) (*x* = 0, 0.0025, 0.0050, 0.0100, 0.0250 and 0.050) were prepared by massing and ball milling the calculated stoichiometric weight of initial oxide precursors. The massed precursors were mixed with isopropanol (IPA) and milled with ytrria-stabilized zirconia (YSZ) grinding media in Nalgene jars using speed controlled rollers. The milling time was usually between 15 to 20 hours to achieve the desired particle size ($d_{50} \leq 0.5$ μm) and homogeneity. The homogenous powder slurry was filtered and dried in a drying oven for 15 hours. The dried powder was collected and stored in a desiccator until calcination was performed. Table I summarizes the details about the chemicals used for sample fabrication.

Table I. Details about the Chemicals used for Sample Batching

Compound name	Purity (%)	Mesh size	Supplier
Barium carbonate ($BaCO_3$)	99.999	-22	Alfa Aesar
Titanium dioxide (TiO_2)	99.999	-22	Alfa Aesar
Gallium oxide (Ga_2O_3)	99.999	-325	Alfa Aesar
Tantalum pentoxide (Ta_2O_5)	99.999	-325	Alfa Aesar

B. Calcination

Dried powders were calcined at elevated temperatures for specified amount of times to obtain the desired phase in soft powder form as discussed below. The calcination temperature has been based on the phase formation using the BaO-TiO_2 phase diagram[51]. The calcination temperature was systematically studied from the initial BT calcination temperature and gradually increasing the temperature until the desired pure phase was obtained as confirmed by room temperature x-ray diffraction (RTXRD). It is important to note that the calcination temperature increased with increase in DP-(Ga,Ta) in the system. In general, the calcination temperature range of 1250°C to 1300°C and a soaking time of 2 hours were found to be the optimal conditions to obtain soft powders of pure phase

perovskite for easy milling. The milled powders were light pressed, placed on platinum foil and covered with an alumina crucible to avoid any cross contamination during calcination. The calcination process was performed in an air atmosphere with a uniform heating and cooling rate of 5 K/min controlled using a programmable box furnace. After calcination, the calcined pellets were again ball milled in IPA with YSZ grinding media for 15 hours. to eliminate particle agglomerations and to obtain fine calcined powder. The calcined powder slurries were dried and room temperature x-ray diffraction was performed on the powders for phase identification before the subsequent processing step.

C. Sintering

The calcined powders were loaded in a stainless-steel lined die of 30 mm inner diameter and uniaxially cold pressed at 20 MPa to form a pellet of ~ 2 mm thickness. The pressed pellets were packed and sealed in vacuum bags and iso-statically pressed at 170 MPa for 30 mins. The pellets were then placed in platinum foil and covered with an alumina crucible and fired. No binders or sintering aids were used. The sintering was performed out at 1350 to 1500°C depending on the composition (BT at 1350°C and BGT0500 at 1500°C) for 10 hours using 5 $^{\circ}$C/min uniform heating and cooling rates. The density of the sintered pellets was measured using water dispersion method before placing electrodes on the sample and electrically characterizing the material. Table II shows the different compositions of materials fabricated, the concentration of dipole-pairs and the name by which the material is referred to through the remainder of this thesis. Table III summarizes the calcination temperature, sintering temperature and sintering time followed for each of the composition.

Table II. Compositions of Fabricated Material, Concentration of DPs and Sample Identification

S.No	Composition	DP concentration	Sample ID
1	$BaTiO_3$	0	BT
2	$Ba\{[Ga_{0.0025},Ta_{0.0025}]Ti_{0.995}O_3$	0.0025	BGT0025
3	$Ba\{[Ga_{0.0050},Ta_{0.0050}]Ti_{0.990}\}O_3$	0.0050	BGT0050
4	$Ba\{[Ga_{0.0100},Ta_{0.0100}]Ti_{0.998}\}O_3$	0.0100	BGT0100
5	$Ba\{[Ga_{0.0250},Ta_{0.0250}]Ti_{0.950}O_3$	0.0250	BGT0250
6	$Ba\{[Ga_{0.0500},Ta_{0.0500}]Ti_{0.900}\}O_3$	0.0500	BGT0500

Table III. Calcination Temperature, Sintering Temperature and Sintering Time followed for each of the Composition

Sample ID	Calcination temperature (°C)	Sintering temperature (°C)	Sintering time (hours)
BT	1250	1350	10
BGT0025	1250	1400	10
BGT0050	1300	1400	10
BGT0100	1300	1400	10
BGT0250	1300	1500	10
BGT0500	1300	1500	10

D. Electrodes

Sintered pellets were polished to obtain parallel and smooth surfaces. Silver electrodes in the form of a circle were fabricated by applying silver paste (7095 Silver conductor paste) to form multiple contacts on one side and silver paste completely covering the surface on the other side of the polished samples to make the ground plane. After applying the silver electrodes, the pellets were heat treated at 650°C for 30 minutes using a heating and cooling rate of 5°C/min. Figure 9 shows a digital image of a typical capacitor structure with multiple silver electrode contacts used for electrical measurements.

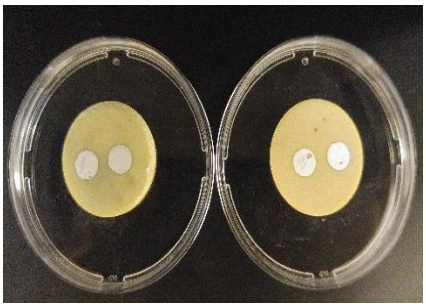

Figure 9. A digital image of a typical capacitor structure with multiple silver electrode contacts used for electrical measurements.

CHARACTERIZATION INSTRUMENTATION

A. Room temperature x-ray diffraction and microstructure:

X-ray diffraction (XRD) was used to characterize the crystal structure and identify phases of both calcined powders and polished sintered pellets for each composition. The diffraction patterns were collected at room temperature using a Bruker D2 Phaser between 20°-80° at a step size of 0.05° and a scan speed of 10°/min using a Cu Kα radiation source and LynxEye^{TM} high speed detector. The microstructural features and grain size were confirmed using a scanning electron microscope (SEM), FEI Quanta 200, on fractured surfaces.

B. Electrical characterization

1. Weak-Field permittivity measurements:

Weak field permittivity measurements, within the frequency range [100 Hz, 1MHz] were conducted on the fabricated capacitive structures. The capacitance and dielectric loss of the materials [-180°C, 195°C] were measured using an HP4284A precision LCR meter, an HP4284A automatic switch scanner and a Delta 9039 temperature controlled chamber. Figure 10 shows the schematic representation of the weak-field permittivity measurement experimental setup. Liquid nitrogen was circulated inside the Delta chamber to cool it below room temperature. For all the measurements, a heating rate of 5°C/min, a hold of 5 min and a step size of 5°C were provided as input parameters within the graphical user interface (GUI) of the LabVIEW equipment control and data acquisition program. The test fixture has four point contacts as illustrated in Figure 11 that are attached to the sample which help to suppress possible signal parasitics. The auto balancing bridge method used for the impedance spectroscopy has advantages of wide frequency coverage of [5 Hz, 40 MHz] and high accuracy over a wide impedance measurement range of [0.01 mΩ, 100 MΩ].

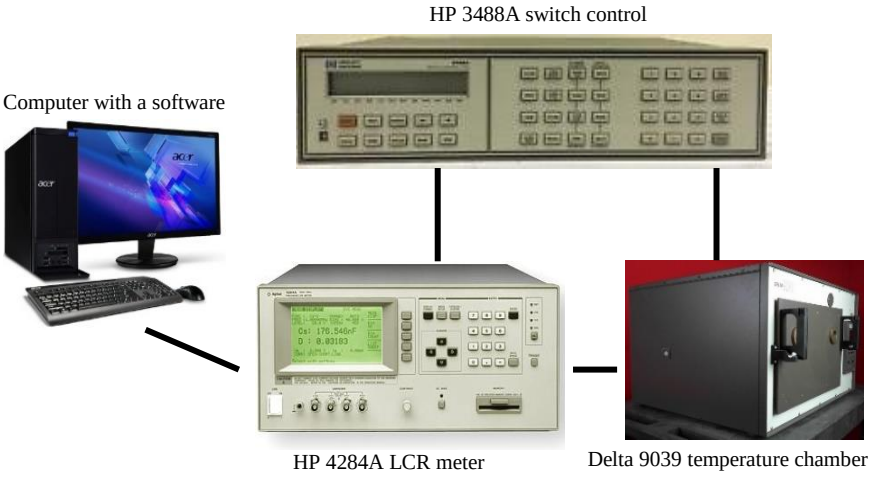

Figure 10. Schematic representation of the experimental setup with temperature range [-190 °C, 195 °C].

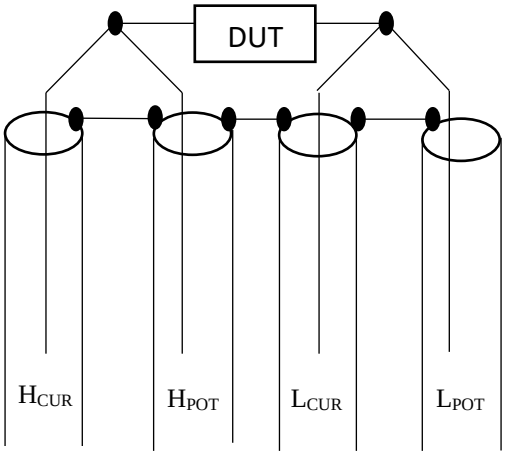

Figure 11. Four-point connection for the device under test[52].

2. Resistivity measurements:

Temperature dependent resistivity of materials were measured from RT to 500°C using a Ney Qex Centurion furnace, a Keithley 6487 picoammeter and voltage source controlled using LabVIEW software with GUI. The applied voltage was set at 10 to 100 V depending on the room temperature resistivity of the material composition. The activation energy and time constant have been calculated using the data plots of

resistivity as a function of temperature. Figure 12 schematically represents the experimental setup for temperature dependent resistivity measurements.

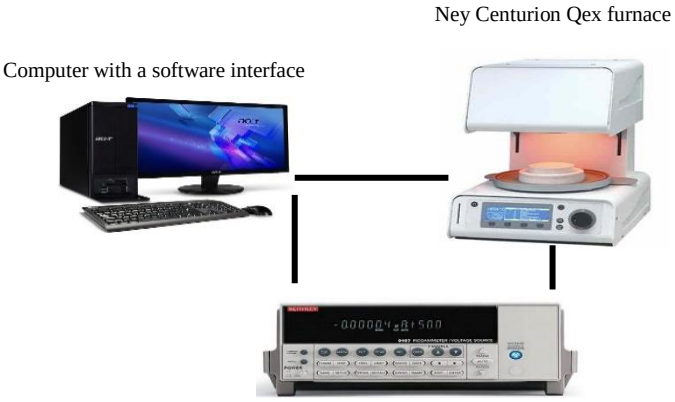

Figure 12. The experimental setup for temperature dependent resistivity measurements.

C. Spectroscopic characterization

X-ray photoelectron spectroscopy (XPS) analyses were accomplished using a PHI Quantera SXM Scanning X-Ray microscope with a monochromatic Al Kα X-ray source (1486.7 eV) of 100 µm beam size and hemispherical electron energy analyzer (HSA). The base pressure of the analyzing chamber was 3 X 10^{-9} Torr and a charge neutralizer at lower energy (< 20 eV) was used throughout analysis. Survey scans of binding energy ranging from 0-1200 eV were performed for elemental identification using parameters: pass energy of 140 eV and step size of 0.5 eV. High-resolution scans were performed over the binding energy range of the identified elements using parameters: pass energy of 26 eV, step size of 0.050 eV and dwell time of 100 ms. The C 1s peak (284.6 eV) was used as an internal standard to correct for the peak shifts due to surface charge accumulation on insulating samples. The obtained survey and high-resolution spectra were processed, curve fit and analyzed using Casa XPS software.

D. Structural characterization

Structural information was obtained using a Bruker D8 Advance System with Anton Paar HTK1200N furnace. A Cu target was used as the radiation source for Kα x-

ray radiation (λ=1.5406 Å). The measurements were performed on powdered samples over a 2-theta range of 20° to 120° and a temperature range from 30°C to 1100°C. Rietveld refinements were performed on the high-temperature x-ray diffraction (HTXRD) data to determine the material lattice constants, coefficients of thermal expansion, unit cell volume and temperature dependent phase transition temperatures.

RESULTS AND DISCUSSION

A. Room temperature x-ray diffraction

RTXRD of samples BT, BGT0025, BGT0050, BGT0100, BGT0250, BGT0500 prepared by solid-state reaction at 1500°C were performed to confirm the perovskite phase formation. No secondary phase formation was identified within the detection limit of the instrument for the DP substitution level of up to x = 0.0500. BT, BGT0025 and BGT0050 show peak splitting in the {200} reflection and can be indexed to *P4m*m space group which is the tetragonal polymorph of pure BT at RT. BGT0100, BGT0250 and BGT0500 show broadening of diffraction peak and can be indexed, within the detection limit of the instrument, to $Pm\bar{3}m$ space group which is the cubic polymorph of pure BT. From RT X-ray diffraction, a transition from tetragonal to pseudo-cubic symmetry appears to occur for the composition close to x = 0.01 and above. Figure 13 shows the room temperature x-ray diffraction patterns of samples BT, BGT0025, BGT0050, BGT0100, BGT0250 and BGT0500

Taking a more detailed look at the XRD data as shown in Figure 13 , the peak near 38° consistently shifts toward lower angle for increasing DP concentration of the solid solutions and indicates volume expansion. The 2θ value for the peak shifts from 39.012° for BT to 38.884° for BGT0500. With the increase in DP-(Ga,Ta) concentration, the *a* lattice parameter increases, the *c* lattice parameter decreases, the overall volume increases and the tetragonality, *c/a*, ratio decreases. At RT, the lattice parameters for pure BT are a = 3.9947 Å and c = 4.033 Å as compared to the lattice parameters of BGT0050 of a = 4.001 Å and c = 4.026 Å. For pseudo-cubic symmetry, the lattice parameter increases with increasing DP-(Ga, Ta) concentration. The volume expansion of DP substituted BT compared to BT even at a very low concentration level of x = 0.0025 is significant and may be due to strain induced in the crystal structure because of the long-range dipole-like interactions induced by DP's in the BT matrix.

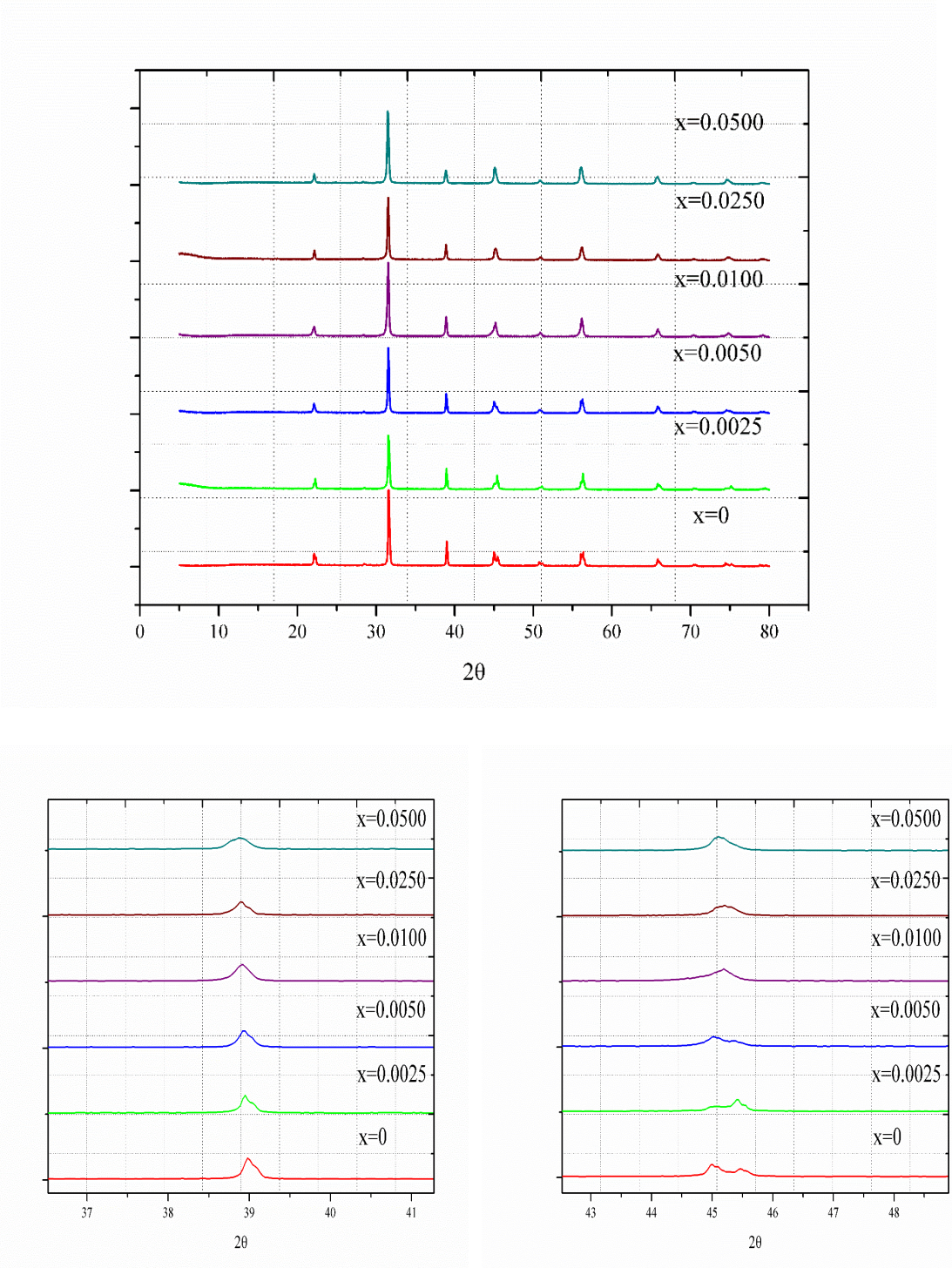

Figure 13. Room temperature x-ray diffraction patterns of BT, BGT0025, BGT0050, BGT0100, BGT0250 and BGT0500.

B. Microstructure

Cold iso-statically pressed powder compacts of ~ 60% of the theoretical density were sintered at 1500°C for 8-10 hours. The densities of the sintered pellets calculated by Archimedes principle are ~ 95% or greater of the theoretical density for each of the compositions. The sintered ceramics consist of randomly oriented grains. The microstructure of BT shows exaggerated grain growth with the grain size ranging from 10-15 μm. In contrast, DP-(Ga, Ta) substituted BT exhibits limited grain growth with fine-grained microstructure. The DP-(Ga, Ta) substituted BT microstructures are comprised of fine grains with a narrow grain size distribution with grain sizes of ~ 1-5 μm. Figure 14 shows the scanning electron microscope images of BT, BGT0025, BGT0050, BGT0100, BGT0250 and BGT0500. Donor rich and acceptor rich compositions exhibit different grain growth mechanisms and recent work by Yoon et al. suggests that in donor rich compositions, donors are likely to inhibit the grain growth whereas acceptor rich compositions exhibit exaggerated grain growth. Although, the DP-(Ga, Ta) substituted BT were prepared with stoichiometrically equal amounts of acceptors (Ga^{3+}) and donars (Ta^{5+}), the microstructure is characteristic of donor rich compositions. Therefore, it is assumed that the grain growth is controlled by Ta^{5+} to some extent in DP-(Ga, Ta) substituted BT. Table IV summarizes the calculated density and the average grain size of BT, BGT0025, BGT0050, BGT0100, BGT0250 and BGT0500.

Table IV. Calculated Density and the average Grain Size of BT, BGT0025, BGT0050, BGT0100, BGT0250 and BGT0500

Sample ID	Density (%)	Grain size (μm)
BT	>90	~ 10
BGT0025	>93	~ 3-5
BGT0050	>95	~ 2-3
BGT0100	>95	~ 2-3
BGT0250	>95	~ 1-3
BGT0500	>95	~ 0.5-1

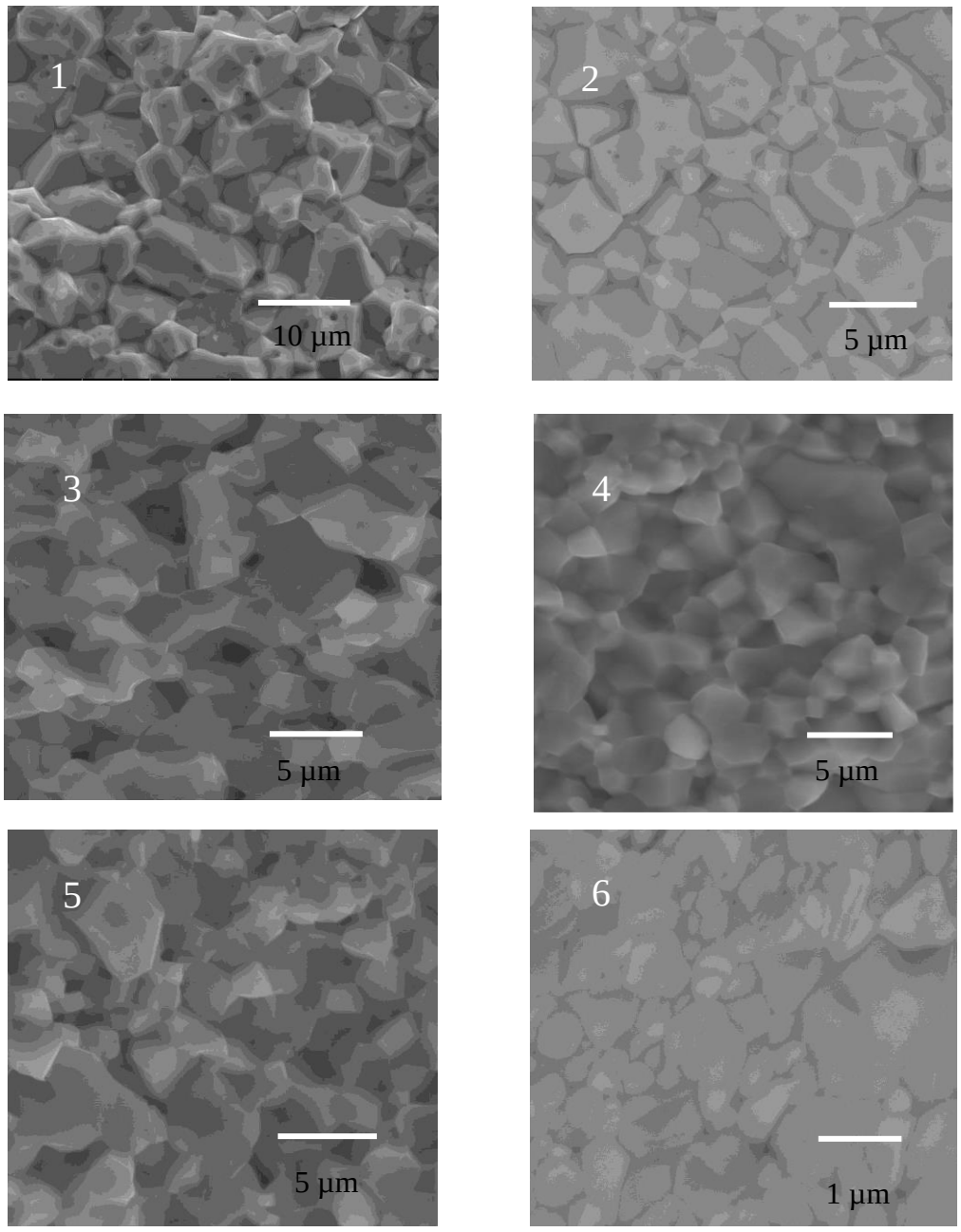

Figure 14. Scanning electron microscope images showing the microstructure of BT (1), BGT0025 (2), BGT0050 (3), BGT0100 (4), BGT0250 (5) and BGT0500 (6).

C. Weak field relative permittivity measurements

The measured frequency and temperature dependent ε_r and dissipation factor of as prepared BT is shown in Figure 15. As discussed before, pure BT exhibits three distinct ε_r maximum at -70°C, 17°C and 131°C which correspond to orthorhombic to rhombohedral (O-R), tetragonal to orthorhombic (T-O) and cubic-tetragonal (C-T) phase

transitions, respectively. The C-T phase transition also known as the Curie temperature (T_c) shows the maximum ε_r and the lowest dissipation factor (tan δ) value when compared to the other two accompanying phase transitions. In general, due to the domain wall motion within the ferroelectric temperature region, ferroelectric materials possess higher losses than in the paraelectric phase. The maximum ε_r value for BT exceeds 15000 and the T_c is at ~131°C. It is important to note that the properties of BT in general are a combined result of many factors such as purity of the raw materials, grain size, sintering temperature, etc. Above 150°C, the sharp increase in tan δ occurs due to thermal conduction mechanisms which dominate at higher temperatures. Since all the materials in this work are BT based, capacitance measurements have been performed over the temperature range [-180°C, 195°C].

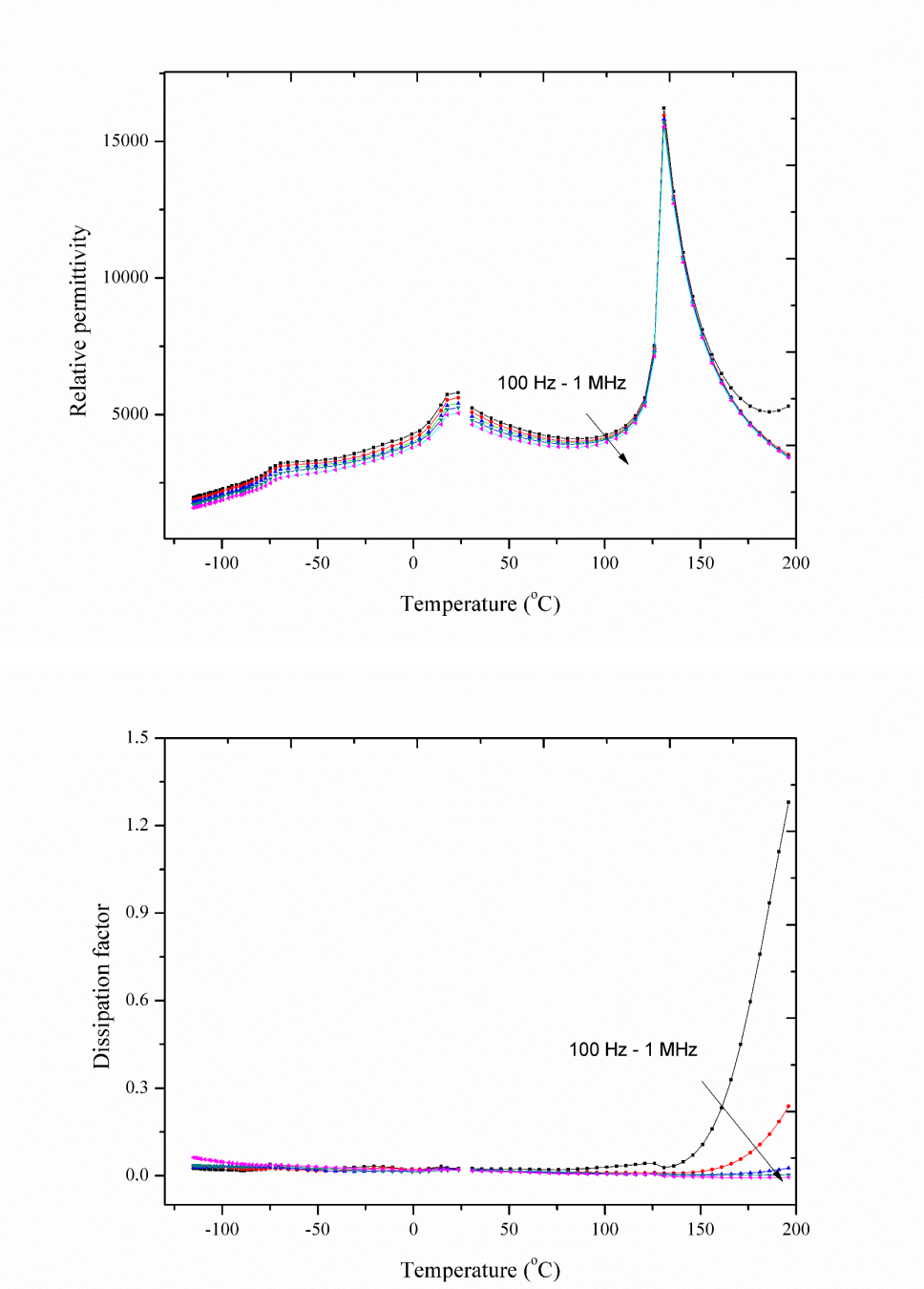

Figure 15. For BT, ε_r (top) and tan δ (bottom) as a function of frequency [100 Hz to 1 MHz] within the temperature range [-100°C, 195°C].

Figure 16 shows the ε_r and tan δ of BGT0025 as a function of frequency within the temperature range [-180 °C, 195 °C]. From the figure, it is apparent that addition of 0.25 mole% of DP-(Ga-Ta), dipole pairs, decreases the T_c to ~ 110°C and stabilizes the T-O phase transition at ~ 17°C when compared to ~ 131°C and 17°C for BT,

respectively. In comparison to the behavior of these materials, BGT*x* with x = 0, 0.0025, 0.005, Zr-doped BT[53] has all the three phase transitions merge at one point at a doping level of ~ 15 at% resulting in a ferroelectric relaxor behavior. For BGT*x* with x = 0.0025, there is some evidence for an O-R phase transition which may be seen as a relatively small rise in permittivity at about -50°C; however, for the sake of simplicity here, only the T-O and C-T phase transitions will be considered further in the discussion.

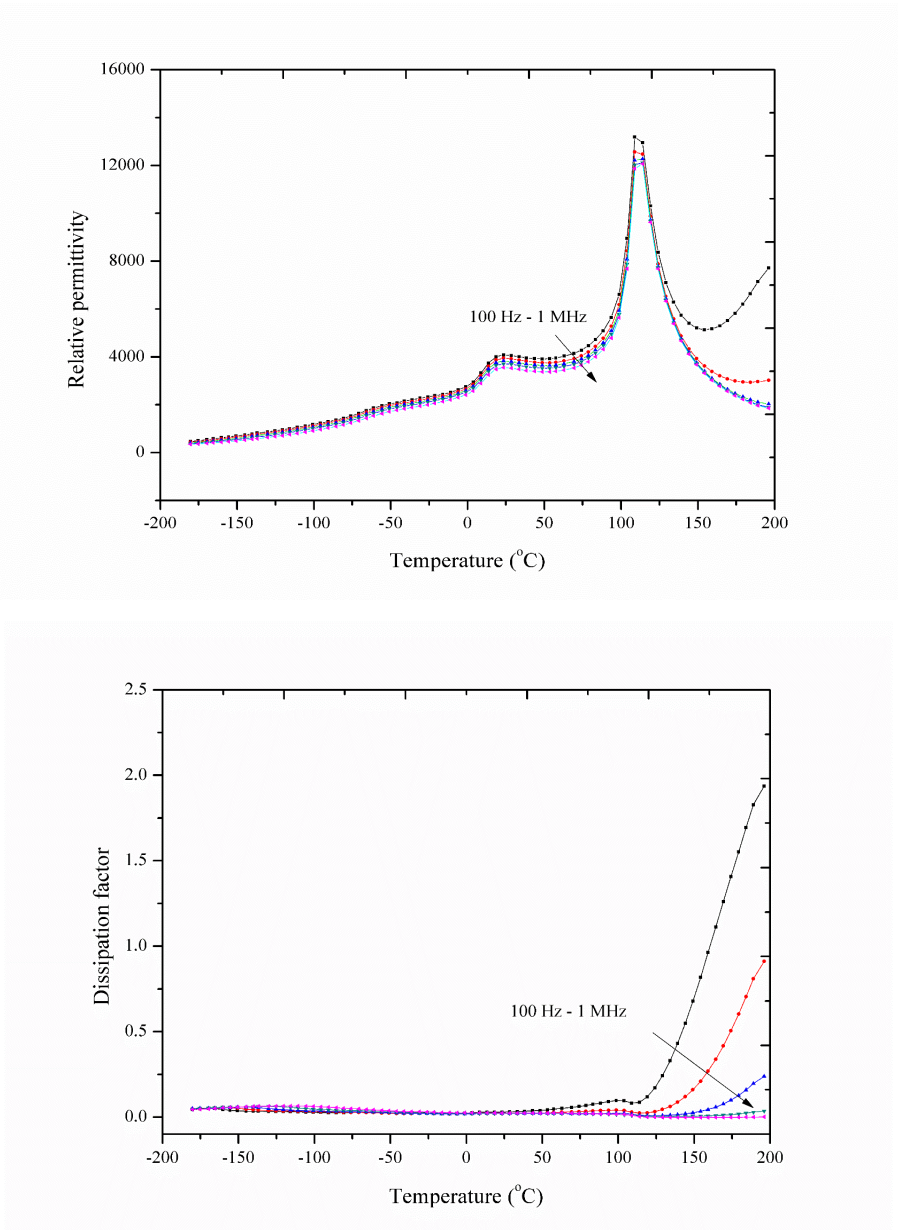

Figure 16. For BGT0025, ε_r (top) and tan δ (bottom) as a function of frequency between the temperature range [-180°C, 195°C].

Further increasing the DP-(Ga-Ta) to 0.5 mole%, decreases the maximum ε_r value from ~ 13000 to ~ 10000 at a frequency of 10 kHz. Figure 17 shows the ε_r and tan δ of BGT0050 as a function of frequency within the temperature range [-180°C, 195°C]. At 0.5 mole% concentration of DP-(Ga,Ta), the T_c of ~90°C has shifted to a little lower temperature when compared to BGT0025 of ~110ºC. The low temperature shoulder at ~20°C appears to be the T-O phase transition. The ε_{max} and tan δ consistently decrease with an increase in DP-(Ga,Ta) concentration. The tan δ is less than 0.05 for the temperature range [-180°C, 195°C]. It is very interesting to note that increasing the DP concentration does not appear to have an effect on the T-O phase transition temperature and has only a minor effect on the C-T phase transition temperature, T_c. In other words, for 0.5 mole% of DP substitution the phase transition temperature remains roughly that of BT yet there is increased diffusivity in the response of ε_r. These results are consistent with the construct proposed by Crown et al.[48] that the charge compensated dipole pairs in the ferroelectric material will result in diffusivity of ε_r while essentially not affecting the phase transition temperature(s) of the parent matrix, BT, material. The work of Crown et al. also mathematically relates the change in slope of the ε_r curve in the paraelectric regime to the increase in DP concentration; however, such analysis appears to be inconsistent with the experimental results presented here.

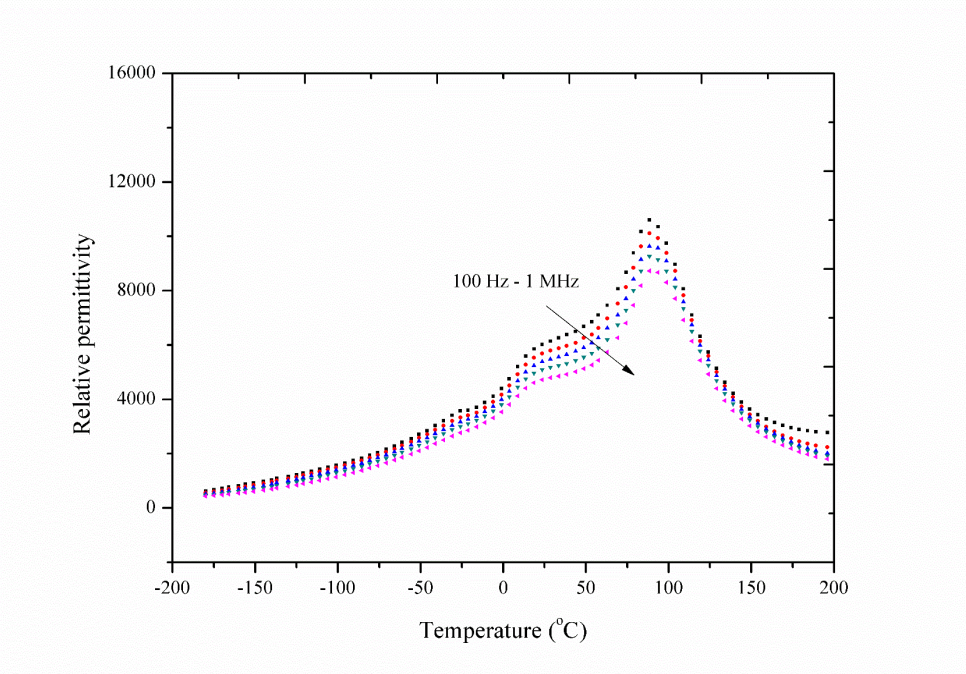

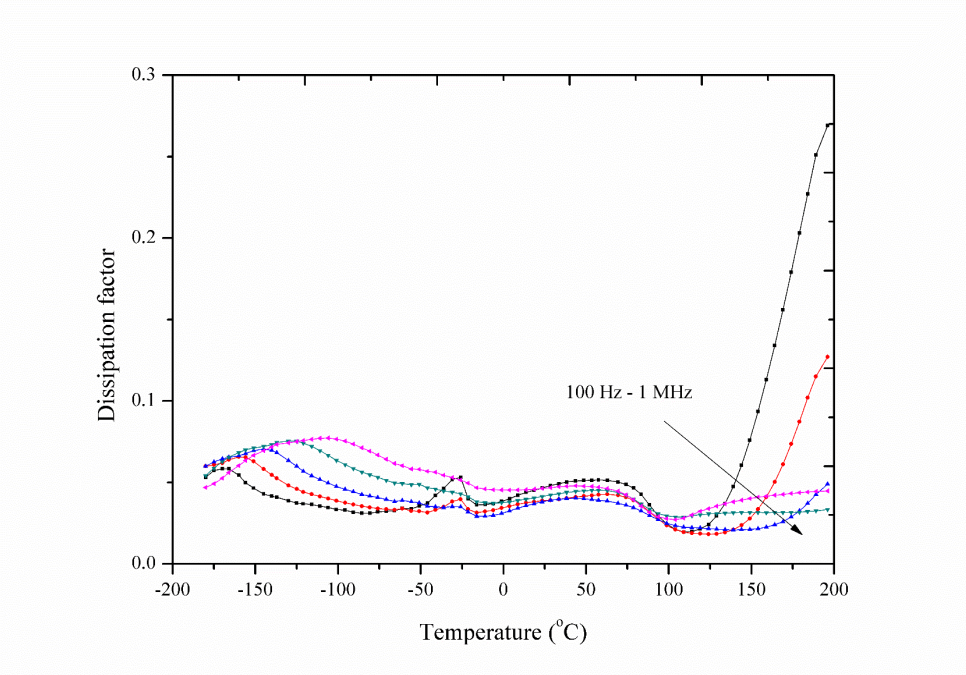

Figure 17. For BGT0050, ε_r (top) and tan δ (bottom) of BGT0050 as a function of frequency between the temperature range [-180°C, 195°C].

Upon further increasing the DP-(Ga,Ta) to 1 mole%, the ε_r maximum decreases further to ~ 9500 at a frequency of 10 kHz. Figure 18 shows ε_r and tan δ of BGT0100 as a

function of frequency within the temperature range [-180ºC, 195ºC]. The dielectric response shows a diffuse peak with T_m at ~17 ºC. Based on the ε_r response as a function of DP concentration, it is conceivable that T_m may be a result of an O-T phase transition and the broad shoulder between the temperature range [90ºC, 150ºC] may be the T-C phase transition temperature, T_c. Characterization results supporting such an unusual behavior of the location of ε_r peaks are discussed within the resistivity and high temperature X-ray diffraction (HTXRD) sections. Conventionally, T_m in the ε_r response is always greater than the Curie temperature, T_c, in the relaxor ferroelectric material[36]. If in fact, here, $T_m < T_c$, this would to the best of our knowledge be first such report of a material possessing $T_m < T_c$.

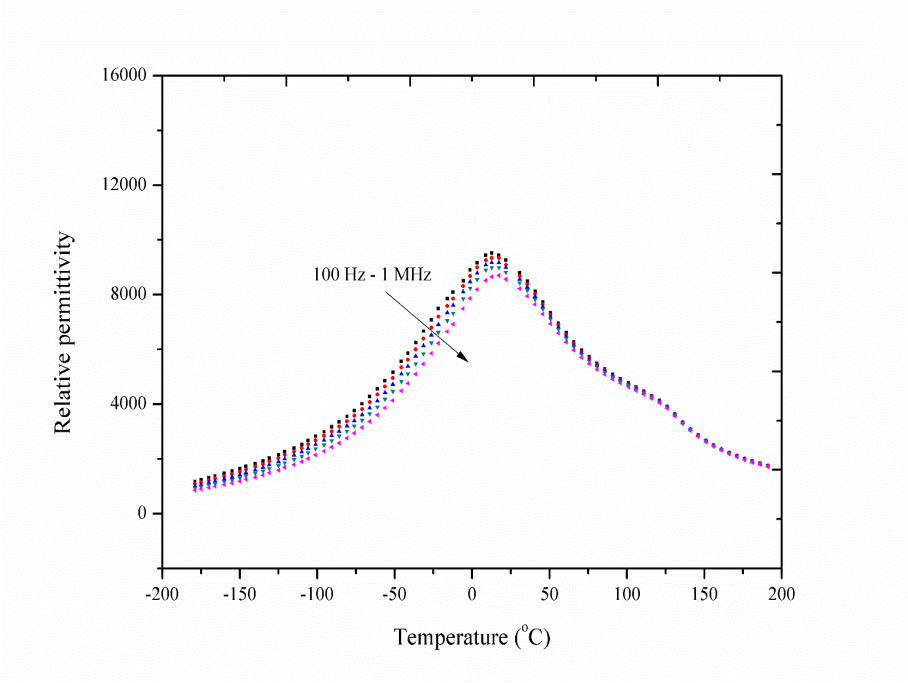

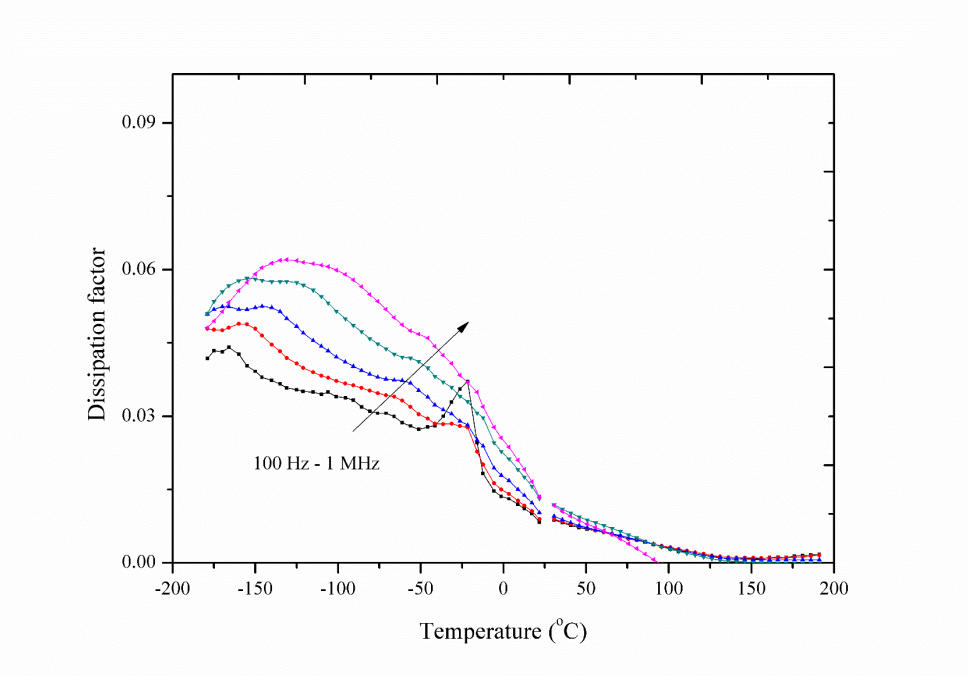

Figure 18. For BGT0100, ε_r (top) and tan δ (bottom) as a function of frequency between the temperature range [-180°C, 195°C].

Upon increasing the DP-(Ga,Ta) concentration to 2.5 mole%, the dielectric response begins to exhibit characteristics similar to relaxor-like behavior. In other words, T_{max} shows strong dispersion as functions of both temperature and frequency. Figure 19

shows the ε_r and tan δ of BGT0250 as a function of frequency [100 Hz to 1 MHz] within the temperature range [-180°C, 195°C]. However, the relaxation at such a low temperature, less than -100°C, is unusual and is not associated with conventional domain wall relaxation[37]. Perhaps the strong relaxation that occurs below about -100°C, where relaxation freeze out should occur, is due to a high enough concentration of random DP-(Ga,Ta), acting as a regional inhomogeneity in the material which results in relaxor-like behavior. Due to temperature limitations of the available x-ray diffraction system, structural investigation in this low temperature regime was not possible. The relaxation in these materials at -100°C and 10 kHz may not be a result of the inhomogeneity associated with typical relaxors but may be due to quenched or random electric field interactions. Also, note that there appears to be a local maximum of ε_r at about 125°C.

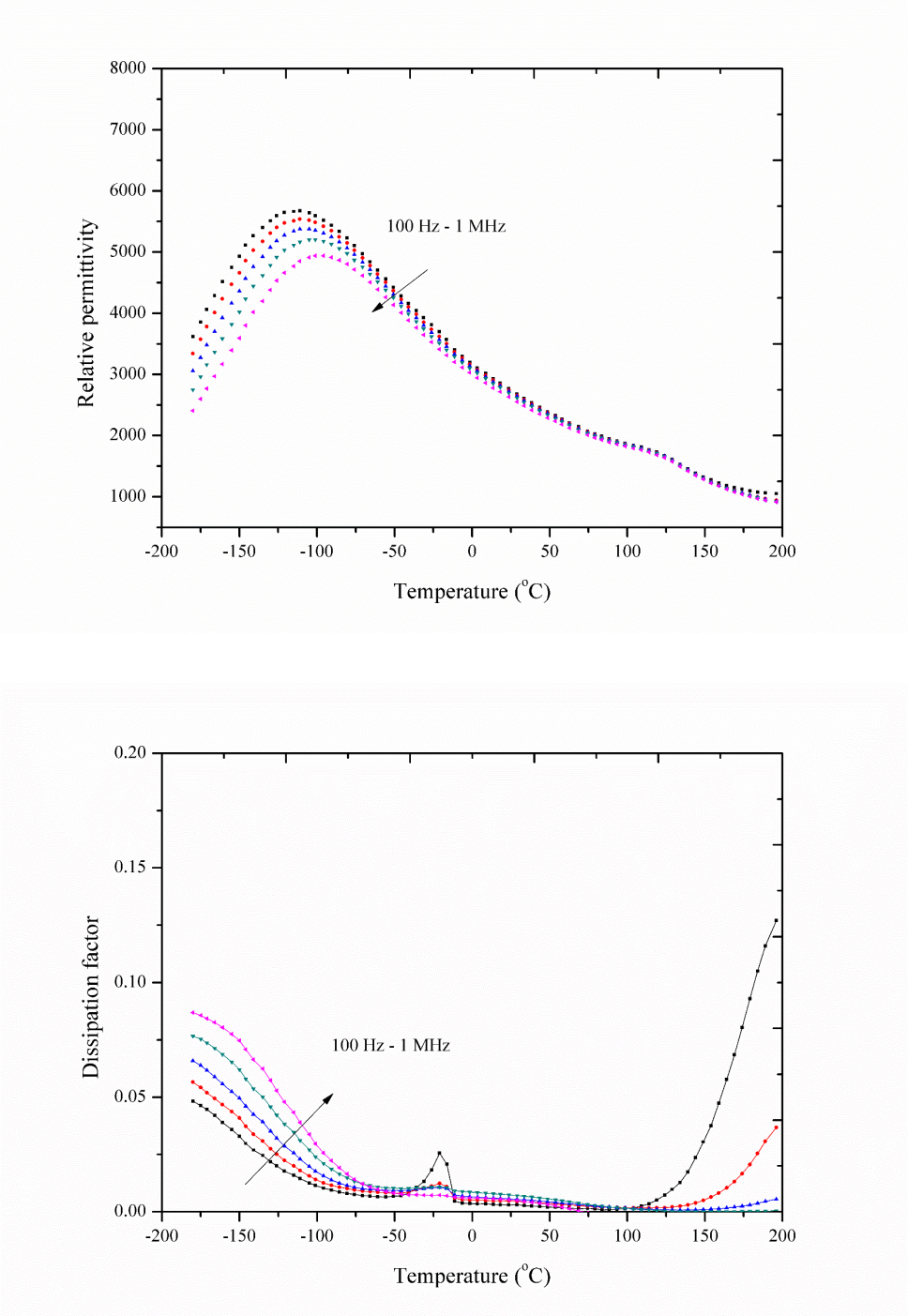

Figure 19. For BGT0250, ε_r (top) and tan δ (bottom) of BGT0250 as the function of frequency between the temperature range [-180°C, 195°C].

At 5 mole% of DP-(Ga,Ta), the ε_r value drops several orders of magnitude to 500 at RT compared to the other materials with lower DP concentrations. There is good

temperature stability of the ε_r response with a mean value of 700 and a deviation of < 20% over the temperature range [RT, 190°C]. There is also a recent report that these materials possess a normalized electric field tunability of about 10% at 1 μm/V while being relatively temperature insensitive[54]. The material exhibits a low loss tangent of less than 0.005 within the temperature range of [-50°C, 150°C] at a frequency of 10 kHz. Figure 20 shows the ε_r and tan δ of BGT0500 as a function of frequency [100 Hz to 1 MHz] within the temperature range [-180°C, 195°C]. While a peak in ε_r could not be observed at the lowest possible temperature of -180°C of this experiment, it appears from the high frequency data that T_m is in the vicinity of -200°C. T_m is projected to be -230°C using the nearly linear decreasing relationship of T_m with increasing concentration of DP's. Note that frequency dispersion of the ε_r is also observed. Further note that there appears to be a small local increase of ε_r at about 125°C.

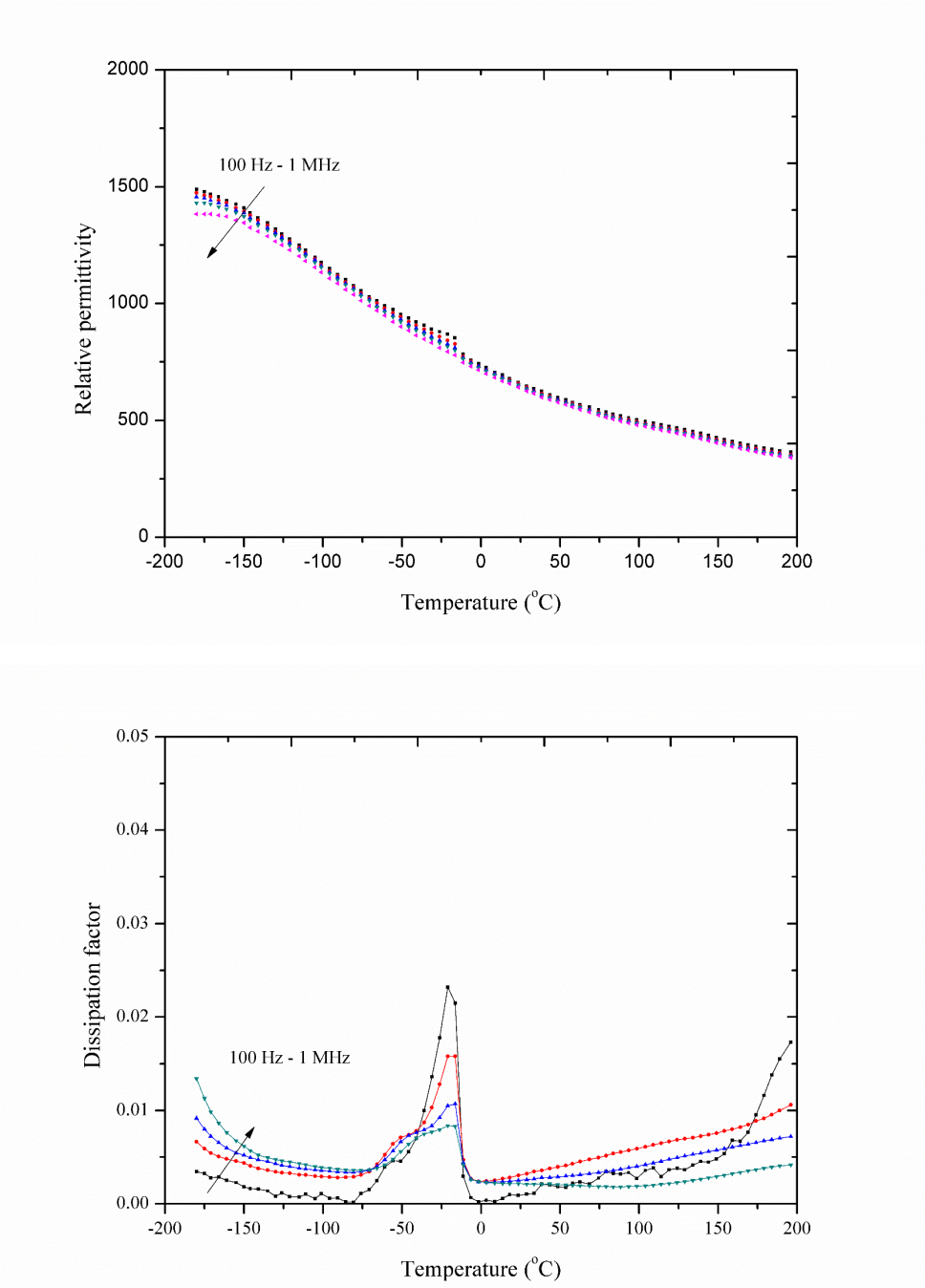

Figure 20. For BGT0500, ε_r (top) and tan δ (bottom) as a function of frequency between the temperature range [-180°C, 195°C].

Figure 21 shows the ε_r response [-180°C, 195°C] at 10 kHz for all of the above discussed compositions. Note that for each composition with $0 \leq x \leq 0.025$, the associated T-O phase transition is about 17°C with little variation in the T_c as a function of DP

concentration. In these materials, it is observed that $T_m < T_c$ that are consistent with HTXRD and resistivity data and will be discussed in the respective sections. This significant observation is different from the existing understanding within the field of ferroelectricity that $T_m = T_c$ is associated with the C-T phase transition in the vast majority (if not in all) the widely studied ferroelectric materials and $T_c < T_m$ in most of the relaxor materials[36]. Further, note that for BGTx with $0 \leq x \leq 0.025$, each exhibits a local maximum in the ε_r at or above 90°C which is fairly close the T_c of pure BT of 131°C. While these effects may be due to core shell structures[49], from processing conditions, such a result appears unlikely. The possible co-existence of phases as well as associated effect on Curie temperature, are further studied and discussed within the HTXRD section along with Rietveld refinement of the x-ray structures. Table V summarizes the observed T_c or T_m, ε_r maximum and ε_r at RT for BT, BGT0025, BGT0050, BGT0100, BGT0250 and BGT050 at 10 kHz frequency.

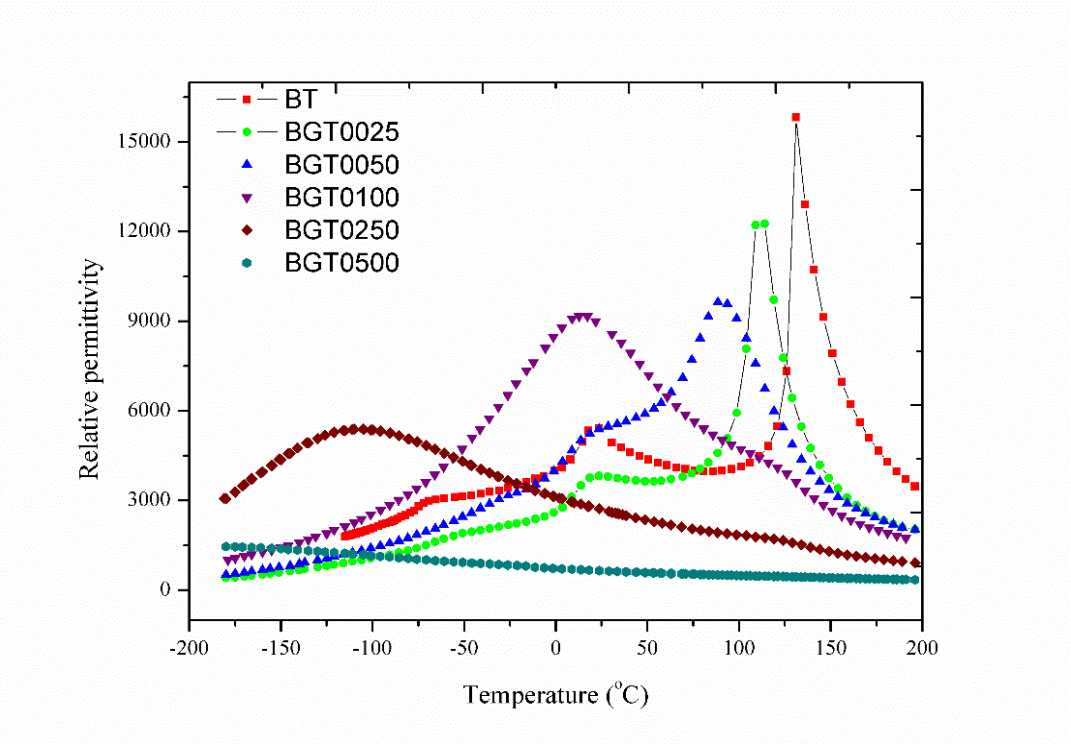

Figure 21. Relative permittivity response between the temperature range [-180°C, 195°C] at 10 kHz for BT, BGT0025, BGT0050, BGT0100, BGT0250 and BGT050.

Table V. Observed T_c or T_m, ε_r maximum and ε_r at RT for BT, BGT0025, BGT0050, BGT0100, BGT0250 and BGT050 at 10 kHz frequency

Sample ID	T_c or T_m (K)	$\varepsilon_{r\ \max}$	ε_r at RT
BT	403	16000	4900
BGT0025	385	12000	3800
BGT0050	363	9700	5600
BGT0100	288	9300	8600
BGT0250	162	5500	2600
BGT0500	NA	1400	700

D. Dielectric relaxation

Relaxation can be defined as a system's monotonous approach to the equilibrium state after excitation. In relaxors, dielectric relaxation is considered in terms of polarization response to the external field of different frequency as the function of temperature[55]. Dielectric relaxation otherwise referred to as diffuse phase transition (DPT) which is quite different from relaxor behavior. A relaxor is characterized by,

- broadening of peaks in the ε_r response as a function of temperature;
- relatively large temperature separation between the maximum of real and imaginary part of dielectric spectrum;
- deviation from Curie-Weiss law near T_m; and,
- strong temperature dependence of ε_r and tan δ as a function of temperature.

Using the above definitions, typical ferroelectric materials follow the Curie-Weiss law, equation (**Error! Reference source not found.**), with classic relaxors deviating from the Curie-Weiss law as quantified using equation (**Error! Reference source not found.**). Experimentally, the Curie constant and Curie-Weiss temperature are determined by linearly extrapolating the $1/\varepsilon_r$ vs temperature (K) graph to the *x*-axis using the high temperature portion of the data. Figure 22 plots $1/\varepsilon_r$ as a function of temperature at 10 kHz for BT, BGT0025 and BGT0050. From the figure it is evident that samples with

0.0025 and 0.0050 mole% of DP-(Ga,Ta) follow the Curie-Weiss law just like a normal ferroelectric material although an increase in diffusivity in the ε_r response is observed when compared to BT. Diffuseness parameters for these materials are listed in Table VI.

It is very important at this point to clearly distinguish relaxors from a DPT materials. The efforts within this thesis demonstrate the ability to induce a DPT in the perovskite structure using the construct of introducing quenched random DP in the parent matrix. These DP's are expected to introduce a dipole-like interaction within the ferroelectric material matrix without interrupting the long-range ferroelectric order. DP's should not act as a region of inhomogeneity. Hence, DP's should neither interfere with the ferroelectric order nor significantly change the frequency and temperature dependence of T_c.

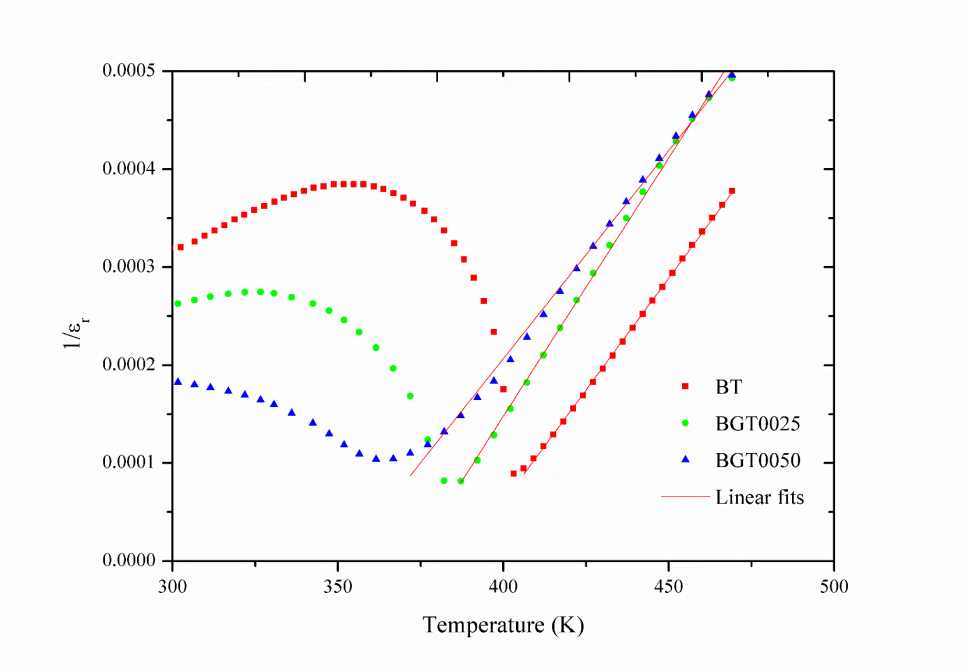

Figure 22. The inverse of ε_r ($1/\varepsilon_r$) as a function of temperature at a frequency of 10 kHz for BT, BGT0025 and BGT0050.

Figure 23 shows the inverse of ε_r as a function of temperature at 10 kHz frequency for BGT0100 and BGT0250. From the figure, it is evident that the materials BGT0100 and BGT0250 has two linear trends. For BGT0100, the linearity in the lower temperature response corresponds to T_m at ~ 5°C in the ε_r response and the region that

follows the Curie-Weiss law at higher temperature corresponds to the local maxima observed at ~ 125°C which is close to the T_c of BT. From the ε_r response and Curie-Weiss law behavior it is doubtful that there is a core-shell structure, although it would be convenient to use the core-shell effect of a BT rich region as the reason for a shoulder at the T_c of BT. The structural and electrical measurements are consistent with the local electric field effect from DP's as discussed below. There are several speculations about the core-shell effect in complex perovskite solid solutions. One such speculation is that the dopants are distributed along the grain boundaries forming a microstructure resembling a core-shell, resulting in separate dielectric response from the core and the shell. Recently, Feteira et al. reported such a core-shell effect to explain that one of the dopants from the DP goes into the BT crystal structure and the other along the grain boundaries forming a core-shell structure[56].

The results of this thesis are at odds with such an explanation for two reasons. Firstly, if one of the dopants goes into the system, and the local maxima is the result of that core, which is a B-site substituted BT rich region, it is expected to shift T_c when compared to pure BT but the local maxima in BGT0100 and BGT0250 is observed at the temperature ~125°C. Secondly, as discussed in detail within the structural characterization section, supporting evidence from HTXRD shows a volume expansion which clearly increases with an increase of DP concentration when compared to BT and suggests that dopants, whether or not they are dipoles, are going into the structure, without leaving a BT inner core, at least within the detection limits of the instrumentation. Several experimental methods: (1) the change of slope in temperature dependent resistivity of the material; (2) the change in slope in the temperature dependent x-ray diffraction measurements; (3) the temperature of peak ε_r; (4) the small shoulder observed in the ε_r response of BGT0100, BGT0250 and BGT0500; (5) structural changes observed by x-ray diffraction for BT, BGT0025, and BGT0050; etc. have been utilized to investigate the dependence of T_c with respect to DP concentration. Using the totality of information from these methods, it appears that T_c reduces as the DP-(Ga,Ta) concentration increases up to a certain concentration level (BGT0025 and BGT0050) and then increases with the further increase in DP-(Ga,Ta) concentration. The increase in T_c for higher DP concentration materials correlates with the NSMM predictions as affirmed

through resistivity and the HTXRD results. The electrical and structural aspects of the materials are discussed in a subsequent section. BGT0050 is not discussed for Curie constant because no T_m was observed within the measurable temperature range.

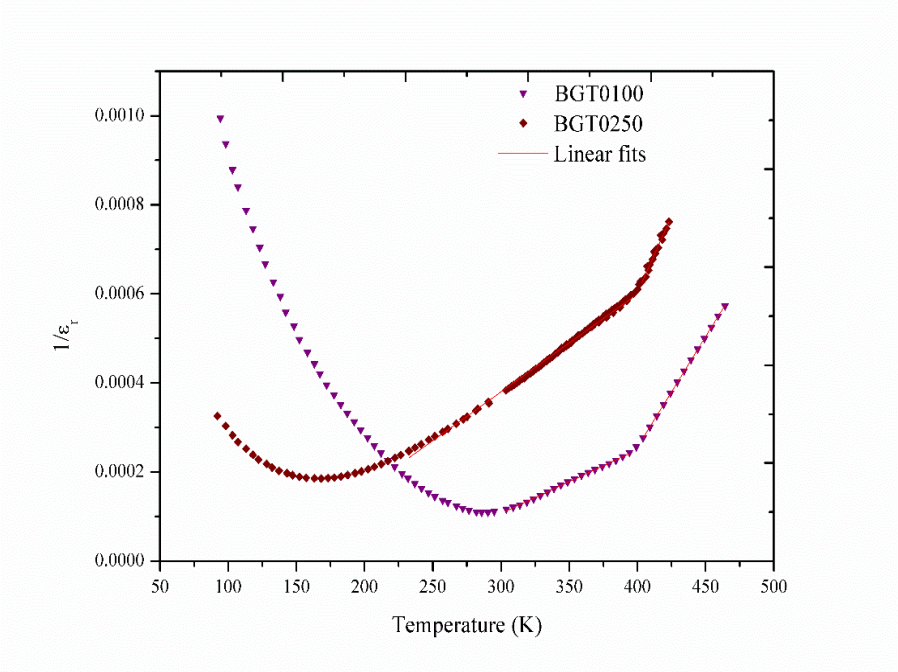

Figure 23. The inverse of ε_r as a function of temperature plot at 10 kHz frequency for BGT0100 and BGT0250.

Figure 24 shows the plots of $\ln(1/\varepsilon - 1/\varepsilon_m)$ versus $\ln(T-T_m)$, and use of equation 15 provides the diffuseness parameter for BT, BGT0025, BGT0050, BGT0100, and BGT0250. A linear relationship is observed for the plotted function of each sample. The slope of each curve yields the diffuseness parameter as listed in Table V, with γ = 1.07, 1.06, 1.8, 1.6 and 1.7 for BT, BGT0025, BGT0050, BGT0100, and BGT0250, respectively. For BGT0050, the fit values range from 1.8 to 2.0, indicating that BGT0050 shows a complete diffuse phase transition. Except for BGT0250, the samples do not show significant deviation from the Curie-Weiss law, which can be used to clearly differentiate DPT from relaxor behavior. BGT0250 deviates from Curie-Weiss law at T_{max}, in the low temperature region, because of the strong dispersion in the ε_r response which is likely the result of DP freezing at that temperature. However, the material BGT0250 obeys the Curie-Weiss law, above the high temperature shoulder, with the Curie constant being reported in Table VI. The reasons for the unusual dispersion have already been discussed

in the previous section. For each of the materials the observed Curie temperature, calculated Curie-Weiss temperature, Curie Constant and diffuseness parameter using the modified Curie-Weiss law are summarized in Table VI.

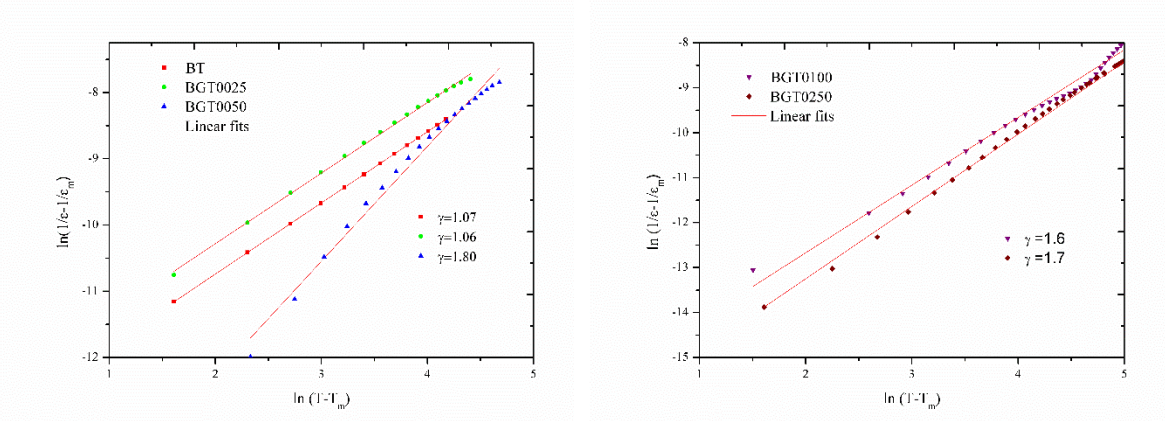

Figure 24. Plots of ln($1/\varepsilon$-$1/\varepsilon_m$) versus ln(T-T_m) for BT, BGT0025, BGT0050 (left) and BGT0100, BGT0250 (right) with inset diffuseness values.

Table VI. The Curie Temperature (T_c), the Curie-Weiss Temperature (T_o), the Curie Constant (C) and the Diffuseness Parameter (γ) for each sample at 10 kHz

Sample ID	T_c (°C)	T_o (°C)	C (X 10^5 K)	γ
BT	131	115	2.18	1.07
BGT0025	112	100	1.90	1.06
BGT0050	91	77	2.41	1.80
BGT0100	N/A	80	2.01	1.60
BGT0250	N/A	28	1.46	1.70
BGT0500	N/A	N/A	N/A	N/A

E. Resistivity measurements

Figure 25 illustrates resistivity as a function of temperature for the samples BT, BGT0025, BGT0050 (left) and BGT0100, BGT0250, BGT0500 (right). The resistivity decreases with increase in temperature which is consistent with semi-conducting behavior of BT-based materials at high temperature. The resistivity decreases slowly up to a specific temperature and drops more rapidly above that temperature. The resistivity is

generally high within the ferroelectric region because of the strong internal macroscopic field resulting from the ferroelectric order acting against the external field and resistivity drops rapidly in the paraelectric region. The fabricated materials fall into two different groups showing: (i) similar behavior compared to BT [Figure 25-(left)]; and, (ii) higher resistivity compared to BT [Figure 25-(right)]. Such behavior can be explained in terms of the DP concentration. A donor or an acceptor dopant generally increases the conductivity by introducing free electrons or holes near the conduction or valence band, respectively. DP's at low concentration create insufficient electric field interaction to overcome the donor or acceptor dopant effects and hence a drop in resistivity of BGT0025 is seen when compared to BT. Once enough DP's are present the internal electric field significantly opposes the applied electric field and the resistivity starts to rise as seen for BGT0050 followed by further enhancement of resistivity for BGT0100. Further increase of the DP concentration to 2.5 and 5 mole% results in a decrease in the RT resistivity by less than one order of magnitude and one order of magnitude respectively, which is an indication that the local DP induced electric field is weaker than the long range electric field within the parent material. The slope of the linear region at high temperature for BT, BGT0025 and BGT0050 falls rapidly when compared to BGT0100, BGT0250 and BGT0500 indicating the later materials possess higher resistivity at high temperature compared to BT as listed in Table VII and illustrates the later materials ability to extend the temperature range of operation of BT-based materials.

The change in slope of resistivity for BT and BGT0025 is an indication of the ferroelectric to paraelectric phase transition which correlates with other electrical and structural measurements. BGT0100, BGT0250 and BGT0500 show an evident slope change in the 130°C to150°C temperature range, near the T_c of BT. Such behavior may be explained in several ways. For instance, at higher temperature, the DP's may start to decouple and act as separate donor and acceptor doped BT resulting in a significant drop in the resistivity or increase in conductivity. The temperature at which resistivity drops may provide some information about the field strength created by DP's of different oxidation states, through the activation energy as well as other parameters. In the future, investigating the effects of DP substituents of different oxidation states by temperature dependent resistivity measurements should assist to better understand DP energies as well

as DP decoupling mechanism(s). Secondly, the activation energy values, slopes of the logarithm of resistivity versus temperature, of DP substituted BT in the paraelectric region are comparable with the pure BT activation energy value. This again supports the idea of charge compensated dipole-like substitution, where the long-range order of BT will remain unaffected while randomly dispersed DP's will induce a DPT.

Figure 26 shows the calculated activation energy within the paraelectric region from the resistivity plots of the samples BT, BGT0025, BGT0050, BGT0100, BGT0250, BGT0500. The activation energy values of all the samples are in reasonable agreement with the calculated and reported BT activation energy value in the paraelectric region[57]. However, note that while the activation energies are similar, the resistivity of lowest concentration of DP substituted BT is shifted to lower temperature while the higher concentrations are shifted to higher temperature. Further note, the break in the slope of the line of the resistivity graphs at about 120°C, 100°C, 85°C, 160°C, 140°C, 135°C, for BT, BGT0025, BGT0050, BGT0100, BGT0250, BGT0500, respectively. Changes in slope of the temperature dependent resistivity plots are often associated with a phase transition; however, as discussed further in the HTXRD section of this thesis, these interesting changes in the slope of temperature dependent resistivity plots may or may not be indicative of the paraelectric to ferroelectric (C-T) phase transition.

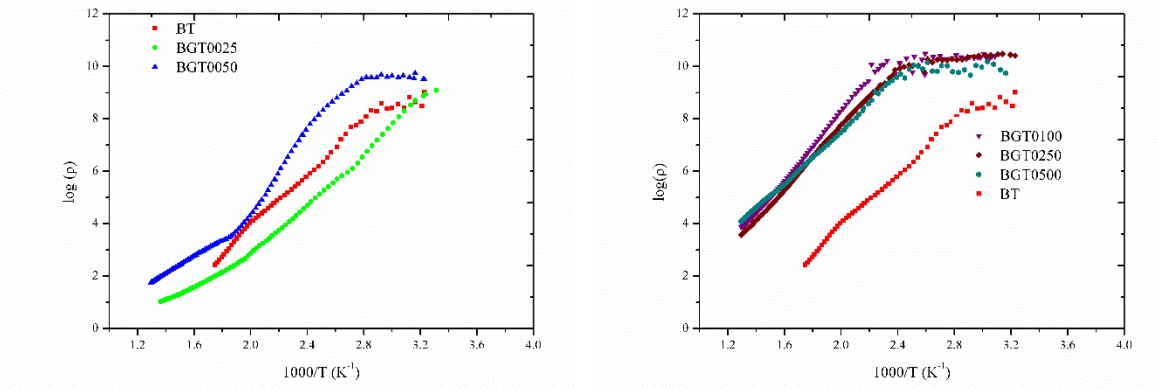

Figure 25. Variation of resistivity as a function of temperature for the samples BGT0025, BGT0050 (left) and BGT0100, BGT0250, BGT0500 (right) with BT included in both plots for comparison.

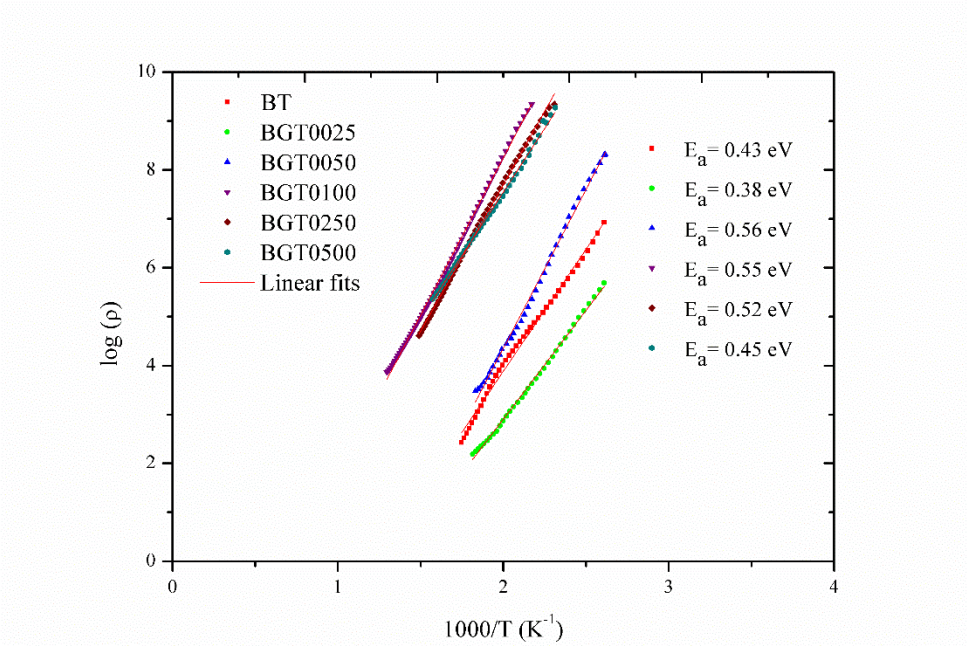

Figure 26. Calculated activation energy within the paraelectric region of the resistivity plots of the samples BT, BGT0025, BGT0050, BGT0100, BGT0250, BGT0500.

Figure 27 shows the RC time constant plotted as a function of temperature for BT, BGT0250, BGT0050 (left) and BGT0100, BGT0250, BGT0500 (right). The increased resistivity and higher ε_r at RT results in a very high RC time constant of about 1900 seconds for BGT0100 as compared with BT at room temperature which has a RC time constant of about ~ 40 seconds. The RC time constant of BT, BGT0250, BGT0050, BGT0100, BGT0250 and BGT0500 at RT are reported in Table VII . Further note that the time constant of BGT*x* with $0.005 \leq x \leq 0.05$ provide at higher temperatures, between 100 and 175 °C, the equivalent time constant as BT at RT.

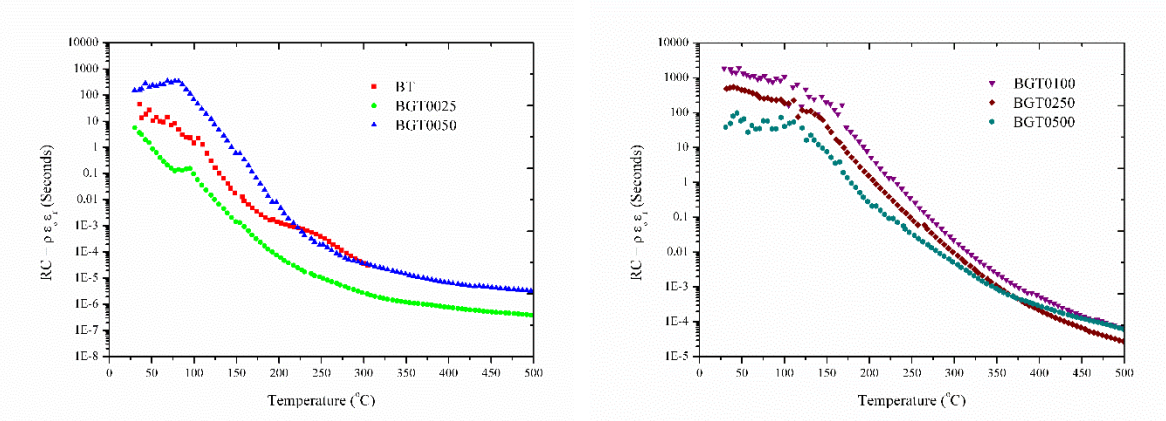

Figure 27. RC time constant plotted as the function of temperature for BT, BGT0250, BGT0050 (left) and BGT0100, BGT0250, BGT0500 (right).

Table VII. Resistivity at RT and 250°C and RC Time Constant at RT for BT, BGT0250, BGT0050, BGT0100, BGT0250 and BGT0500

Sample ID	Resistivity at RT (Ω·m)	Resistivity at 250°C (Ω·m)	Time constant at RT (seconds)
BT	~10^8	~10^3	15
BGT0025	~10^9	~10^2	6
BGT0050	~10^9	~10^3	150
BGT0100	~10^{10}	~10^7	1900
BGT0250	~10^{10}	~10^7	550
BGT0500	~10^9	~10^7	80

F. X-ray photoelectron spectroscopy

The XPS spectrum was used to study the oxidation state of each element in DP-(Ga,Ta) substituted BT because a change in chemical environment of the constituent can influence electrical properties. Figure 28 shows the XPS survey spectrum of BGT0500 for the binding energy range between 0-1200 eV, i.e., for the elements present" Ba, Ti, O, Ga, Ta and C. All survey spectra look similar with the exception that Ga and Ta are not within the detectable limits for $x \leq 0.025$, BGT0250.

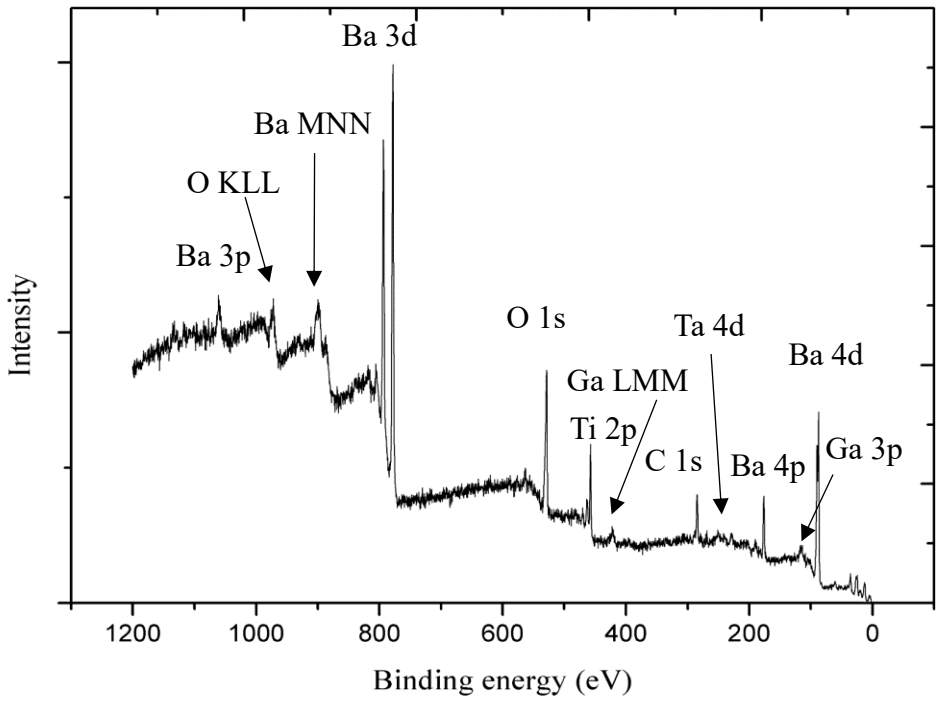

Figure 28. XPS survey spectrum of BGT0500 for the binding energy range between 0-1200 eV.

Figure 29 show Ba 3d XPS spectra of BGT0025, BGT0050, BGT0100, BGT0250 and BGT0500. Curve fits to the BGT0500 spectrum are shown within the inset of Figure 29. From the fit curve, Ba 3d is composed of two components that form the broad peak with a shoulder in the higher binding energy region, ~ 779 eV (±0.5 eV) and another at ~ 778 eV (±0.5 eV). Similarly, but not shown here, the spectra for each of the samples have been analyzed. With reference to Table VIII, the Ba 3d binding energy values of BGT0025, BGT0050, BGT0100, BGT0250 and BGT0500 are reported. The peak at 778 eV corresponds to Ba^{2+} in the perovskite structure and the peak at ~ 779 eV has been reported in the literature to be surface related[58]. The peak at ~ 779 eV is believed to be associated with carbonate species and is consistent with the small peak at ~ 288.4 eV near C 1s peak which is the result of carbonate species in the sample [59]. Figure 32 shows the C 1s spectrum for BGT0500 for reference. The possibility of finding CO_3^{2-} species in the samples synthesized at 1300°C and assignment of this peak to a particular species is still a matter of discussion[60]. Ultimately, these additional peaks, ~ 779 eV and ~ 288.4 eV, are from a combination of factors.

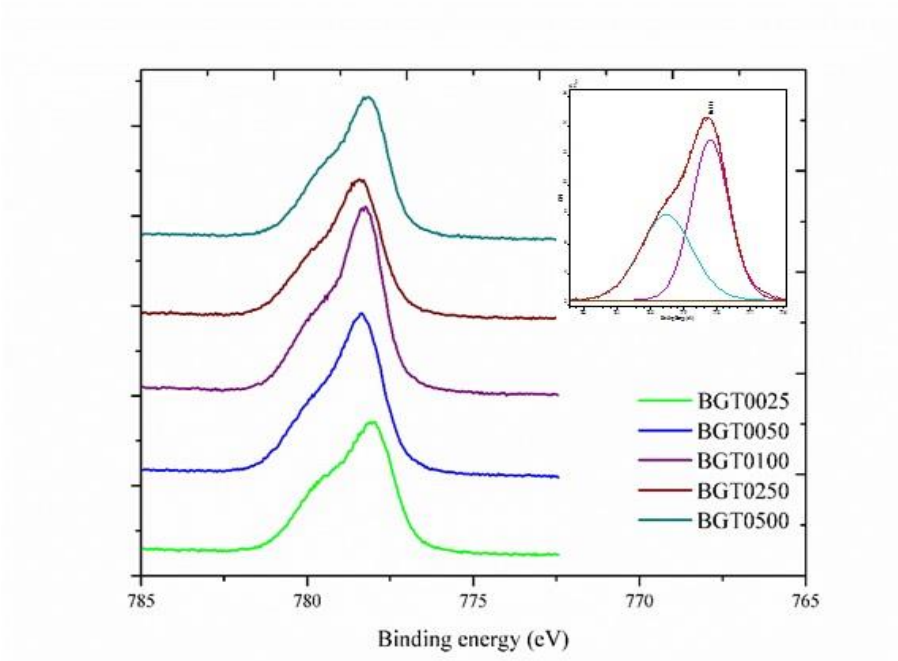

Figure 29. Ba 3d XPS spectrum of BGT0025, BGT0050, BGT0100, BGT0250 and BGT0500. Curve fit to BGT0500 (Figure inset).

The main interest in the present XPS investigation is determination of the oxidation state of Ti because it has been previously reported that an aliovalent Nd dopant addition of as low as 1 at% changes the oxidation state of Ti in the system[61,62]. Determination of the oxidation state of Ti is important for knowing whether the substitutions, Ga^{3+} and Ta^{5+}, for Ti go into the structure of BGTx with $0 < x \leq 0.05$ as dopants or as charge compensated DP's. Figure. 30 shows Ti 2p XPS spectrum of BGT0025, BGT0050, BGT0100, BGT0250 and BGT0500.

Curve fits to BGT0500 have been performed and are shown in the inset of Figure. 30. The spectrum is a combination of two symmetric peaks, one corresponding to Ti $2p_{3/2}$ at ~ 457 eV (±0.5 eV) and the other corresponding to Ti $2p_{½}$ at ~ 463 eV (±0.5 eV). Similarly, but not shown here, the spectra for each of the samples have been analyzed. With reference to Table VIII, Ti 2p binding energy values of BGT0025, BGT0050, BGT0100, BGT0250 and BGT0500 are reported. From the literature, if Ti is in a mixed oxidation state, the Ti $2p_{½}$ state exhibits a broad peak and Ti $2p_{3/2}$ has a shoulder at the lower binding energy[60,62]. The curve fits to the XPS spectrum of Ti 2p show that the Ti is

in a single, +4, oxidation state based on the peak positions. For the relatively high DP substitution levels compared with the detection limit of the technique, there is no evidence of Ti^{3+} features. This result strongly indicates that within detection limits, the characteristics of BGT*x* with $0 < x \leq 0.05$ are consistent with the construct of charge compensated dipole-like substitutions of Ga^{3+} and Ta^{5+} throughout the material system with Ti remaining in +4 single oxidation states in the perovskite structure. Thus, the results are consistent with the hypothesis of randomly distributed DP's throughout the material giving rise to the DPT in the material[63].

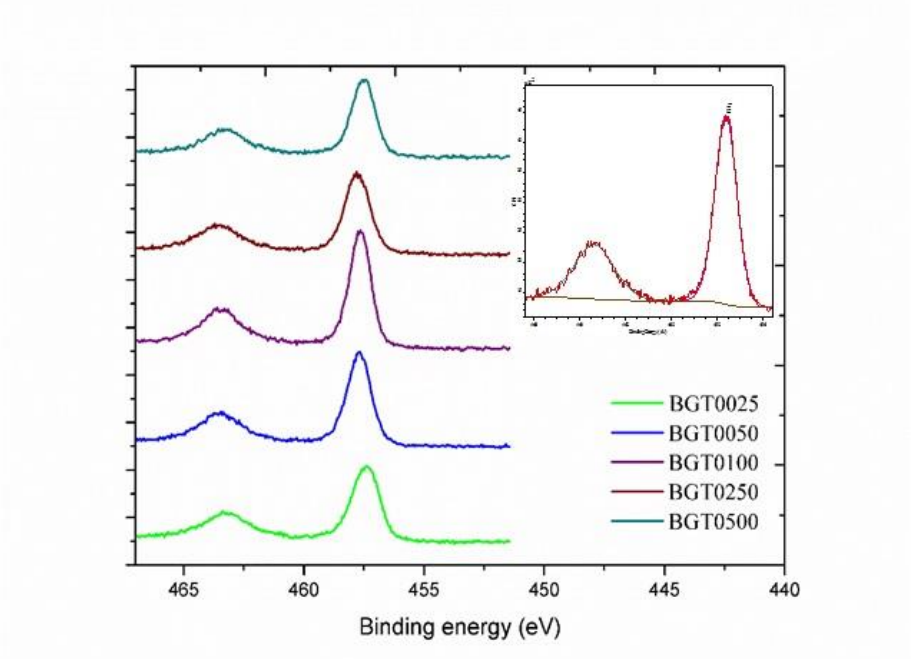

Figure 30. Ti 2p XPS spectrum of BGT0025, BGT0050, BGT0100, BGT0250 and BGT0500. Curve fit to BGT0500 (Figure inset).

Figure 31 shows the O 1s XPS spectra of BGT0025, BGT0050, BGT0100, BGT0250 and BGT0500. Curve fits to BGT0500 are within the inset of Figure 31 . The first peak in the lower binding energy range of ~ 528 eV (±0.5 eV) corresponds to oxygen in the perovskite structure. Similarly, but not shown here, the spectra for each of the samples have been analyzed. With reference to Table VIII, the O 1s binding energy values of BGT0025, BGT0050, BGT0100, BGT0250 and BGT0500 are reported. The peak at ~530 eV (±0.5 eV) is likely due to an OH group or chemisorbed H_2O on the surface of the sample[58].

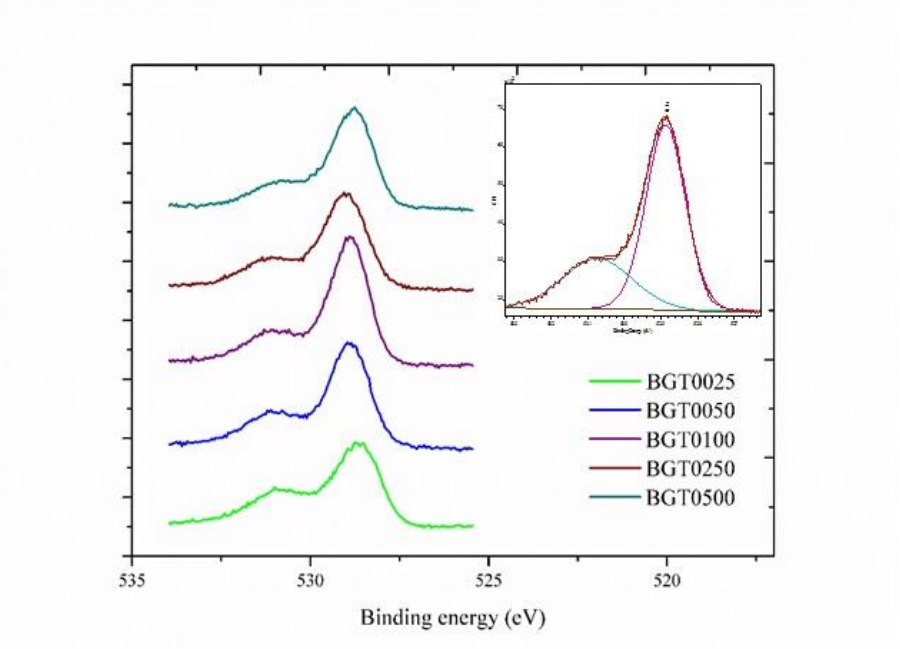

Figure 31. O 1s XPS spectrum of BGT0025, BGT0050, BGT0100, BGT0250 and BGT0500. Curve fit to BGT0500 (Figure inset).

Table VIII. Binding energy (eV) of Ba 3d, Ti 2p and O1s for BGT0025, BGT0050, BGT0100, BGT0250 and BGT0500

Sample ID	Ba 3d (eV)	Ti 2p (eV)	O 1s (eV)
BGT0025	778.00 & 779.55	457.43 & 463.21	528.64 & 530.72
BGT0050	778.13 & 778.96	457.60 & 463.33	528.77 & 530.86
BGT0100	778.08 & 779.49	457.50 & 463.27	528.73 & 530.75
BGT0250	778.21 & 779.69	457.59 & 463.35	528.82 & 530.87
BGT0500	778.19 & 779.51	457.61 & 463.37	528.87 & 530.73

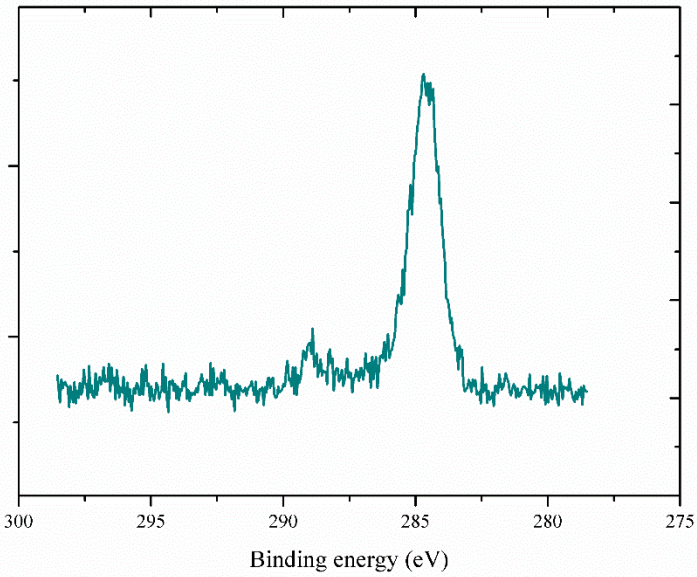

Figure 32. C 1s XPS spectrum of BGT0500.

G. High temperature X-ray diffraction

Figure 33 shows the X-ray diffraction pattern of BT for the temperature range 30°C to 1000°C in air atmosphere at a heating rate of 30 K/min at a step size of 25°C up to 200°C (pattern number 1-8) and a step size of 100°C from 200°C to 1000°C (pattern number 9-16). The same experimental conditions (heating rate and step size) have been utilized to perform temperature dependent x-ray diffraction analysis of BGT0025, BGT0050, BGT0100, BGT0250 and BGT0500. For brevity, the XRD patterns are not included for BGT0050, BGT0100, BGT0250 and BGT0500. The XRD data are discussed and presented in two sets since the samples lie in two distinct categories as discussed in the previous sections. BT, BT0025 and BGT0050, well behaved ferroelectric materials, will be discussed in the first group. BGT0100, BGT0250 and BGT0500, relaxor-like materials, will be discussed in the second group.

Rietveld refinements of the XRD data were performed over the temperature range 30°C to 1000°C using Topas 4.0 XRD data refinement tool. Using the ICDD database search match engine, the initial space group, and the initial lattice parameter at room temperature were estimated to be tetragonal and 4.000 Å, respectively, for BT. Therefore,

initially refinement at each temperature was performed using a cubic lattice parameter, followed by multiple refinements using different space groups for each temperature based on the method of minimizing refinement error. The same procedures as stated above have been followed during refining BGT0025 and BGT0050 to find the tetragonal to cubic phase transition temperature, the lattice dimensions and thermal expansion coefficient. Figures 34, 35, and 36 show the Rietveld refinements at 75°C (top) and 800°C (bottom) of BT, BGT0025, and, BGT0050, respectively, and are representative of the tetragonal and cubic phases as well as goodness of fit to the samples, respectively.

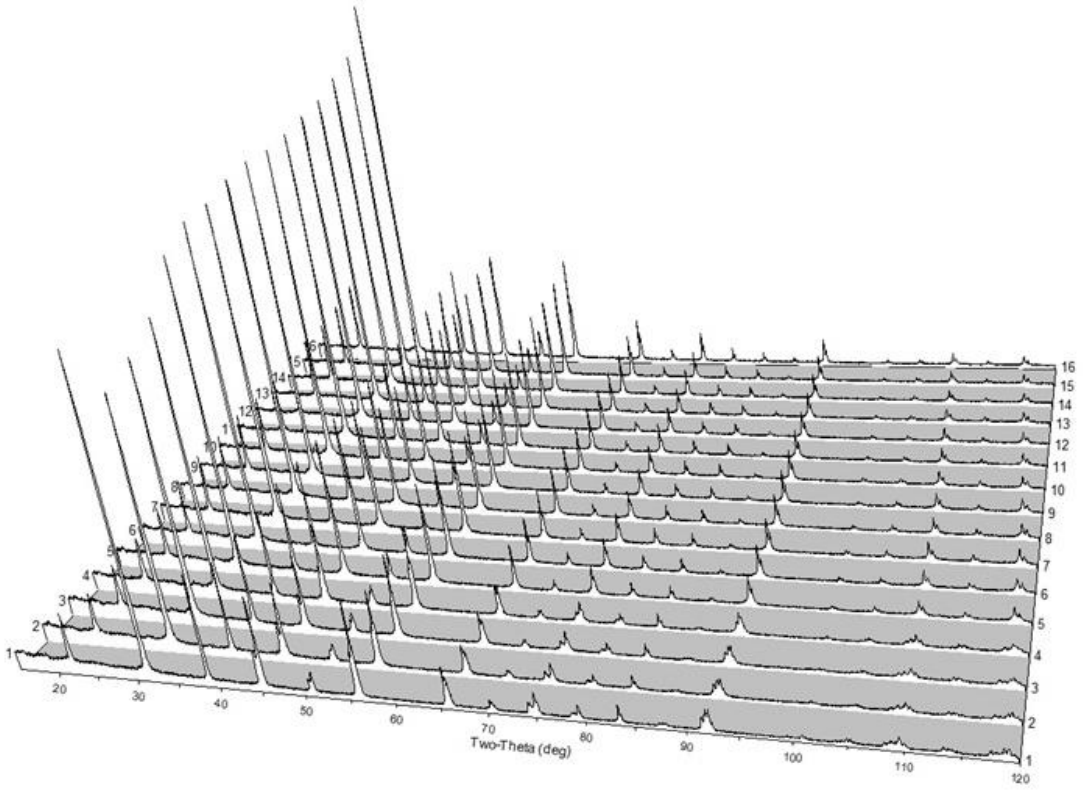

Figure 33. X-ray diffraction pattern of BT for the temperature range 30°C to 1000°C in air atmosphere at a heating rate of 30K/min at a step size of 25°C up to 200°C (pattern 1-8) and a step size of 100°C from 200°C to 1000°C (pattern 9-16).

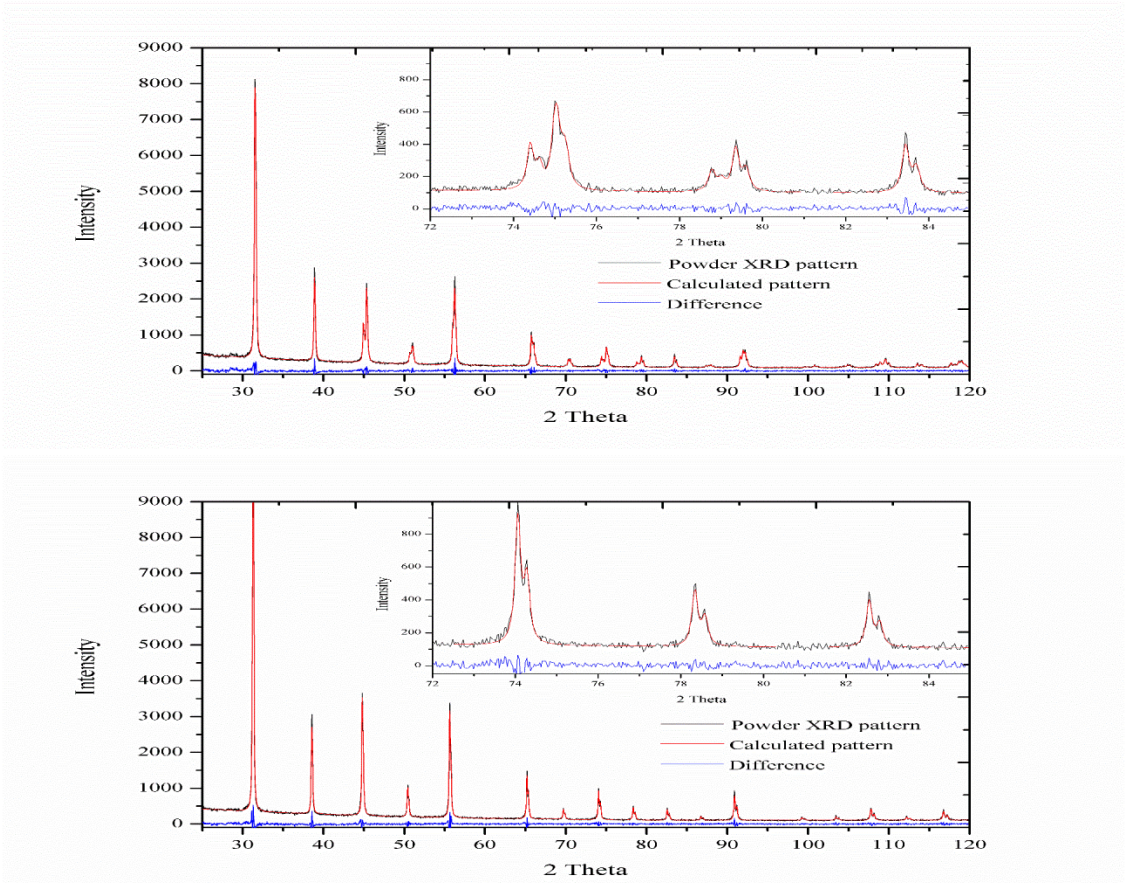

Figure 34. Rietveld refinement of BT at 75°C (top) and 800°C (bottom) illustrate fits to the tetragonal and cubic phases, respectively.

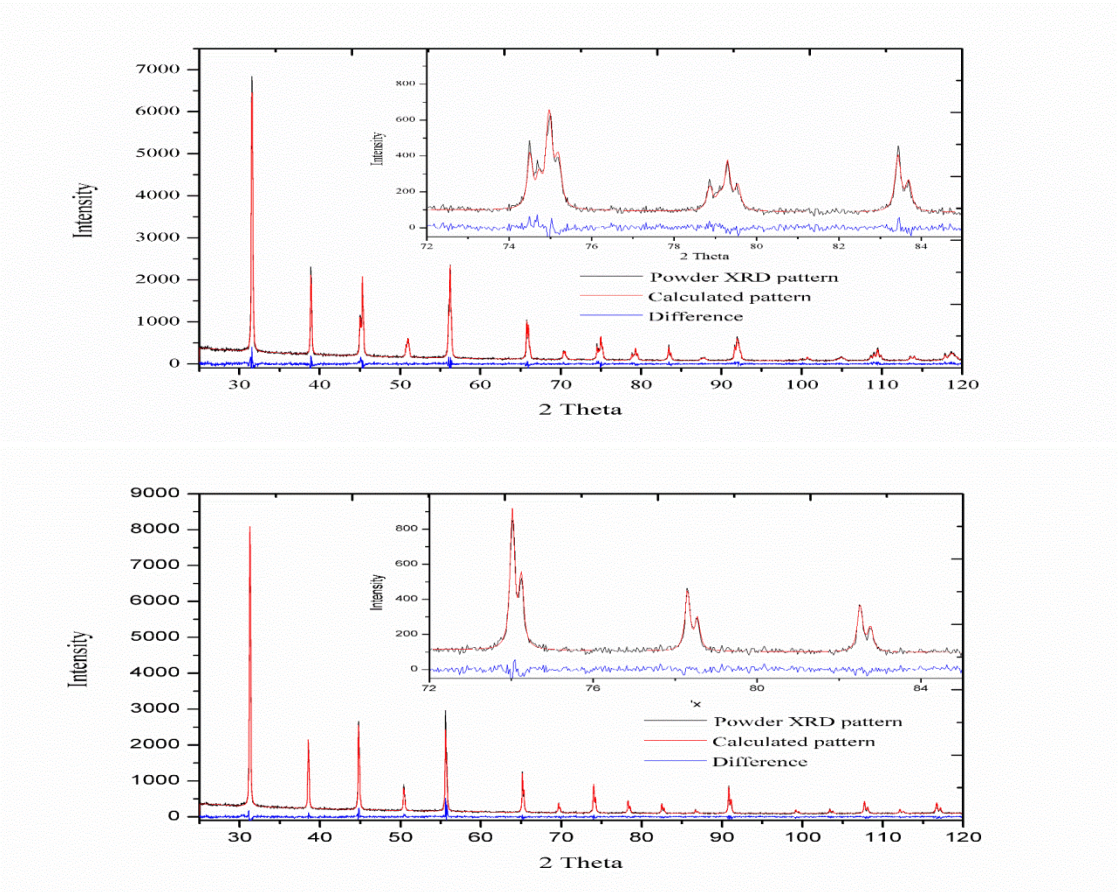

Figure 35. Rietveld refinement of BGT0025 at 75°C (top) and 800°C (bottom) illustrate fits to the tetragonal and cubic phases, respectively.

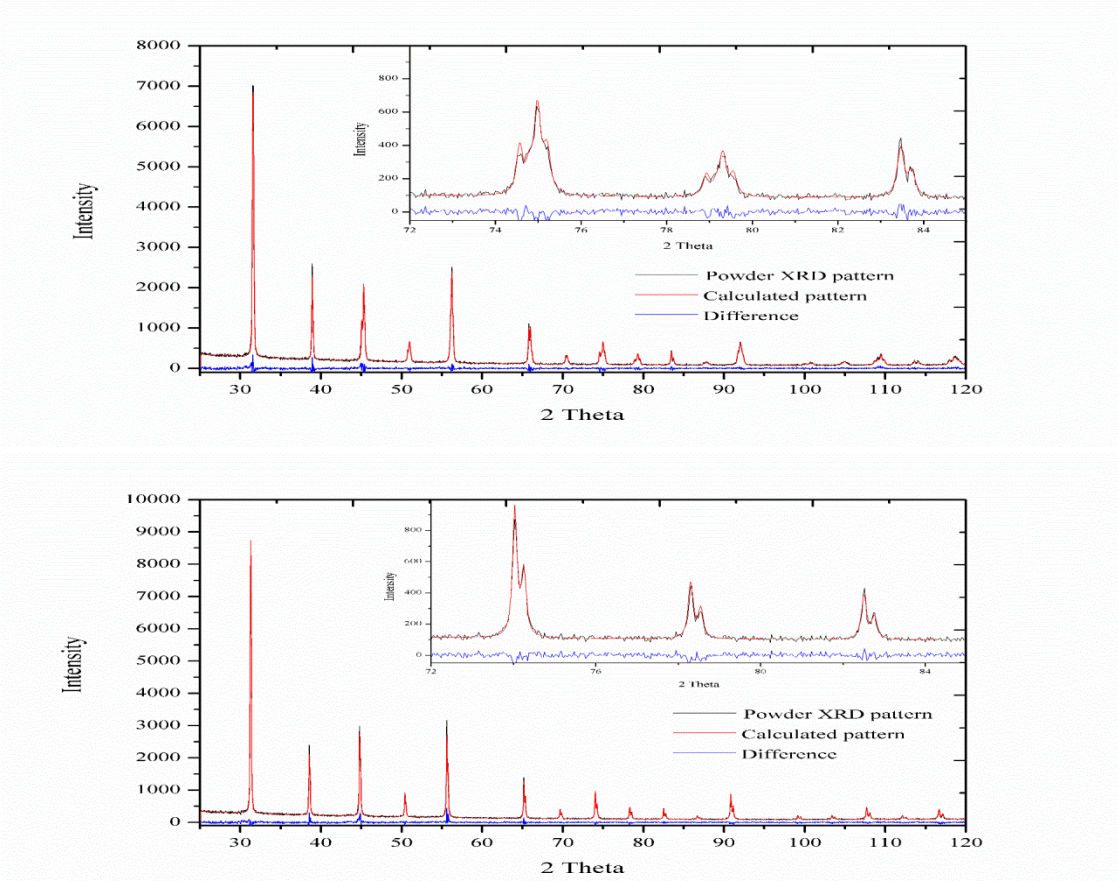

Figure 36. Rietveld refinement of BGT0050 at 50°C (top) and 800°C (bottom) illustrate fits to the tetragonal and cubic phases, respectively.

Figures 37, 38 and 39 show the lattice parameter as a function of temperature with the errors associated for each refined lattice parameter of BT, BGT0025 and BGT0050, respectively. The tetragonal to cubic phase transition, otherwise known as T_c, are observed at 125 °C, between 100°C to 125°C and between 75°C to 100°C for BT, BGT0025 and BGT0050, respectively. The obtained experimental values are in good agreement with the ε_r, resistivity measurements and the literature values. The tetragonal unit cell dimensions at 30°C are a = 3.9948±0.0001 Å and c = 4.0333±0.0001 Å and the cubic unit cell dimension at 300°C is a = 4.0180 ±0.0001 Å for BT. For BGT0025, the tetragonal unit cell dimensions at 30°C are a = 3.9984±0.0001 Å and c = 4.0305±0.0001 Å and the cubic unit cell dimension at 300°C is a = 4.0120±0.0001 Å. For BGT0050, the tetragonal unit cell dimensions at 30°C are a = 4.0011±0.0001 Å and c = 4.0258±0.0001 Å and the cubic unit cell dimension at 300°C is a = 4.0201±0.0001 Å

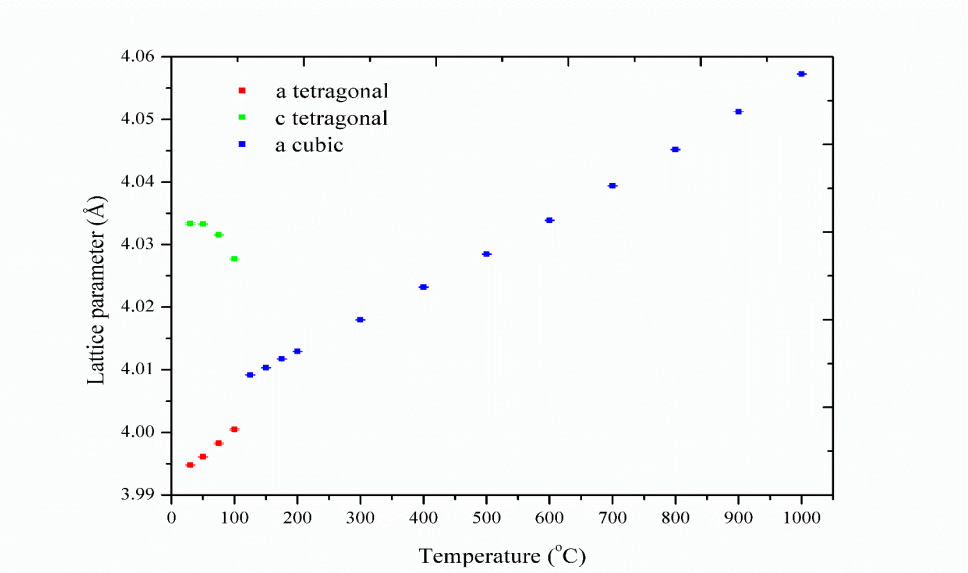

Figure 37. BT lattice parameters as a function of temperature with associated error bars for each refined value.

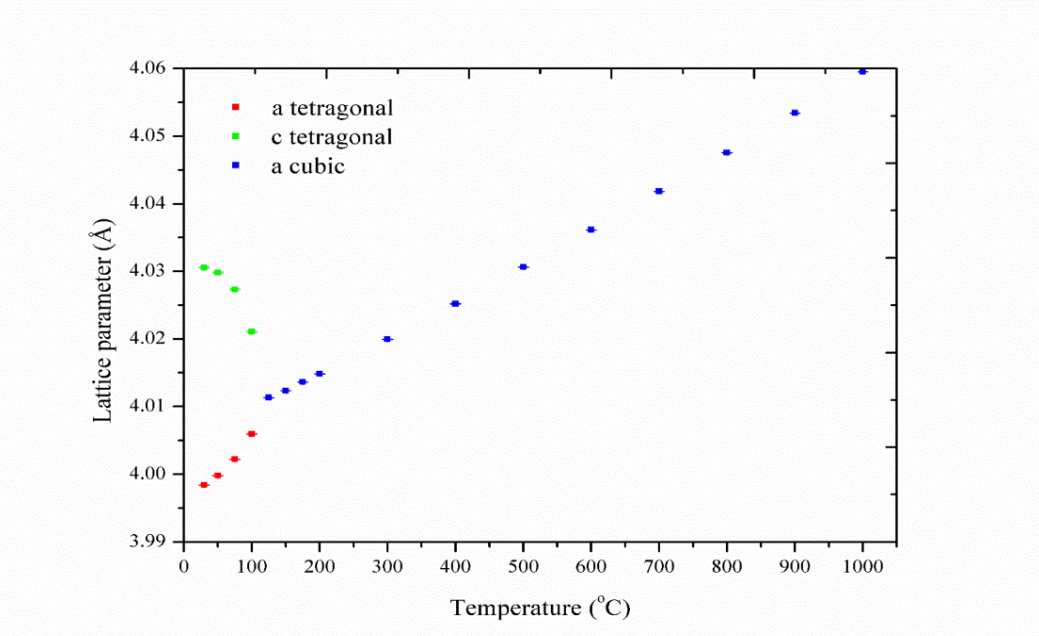

Figure 38. BGT0025 lattice parameters as a function of temperature with associated error bars for each refined value.

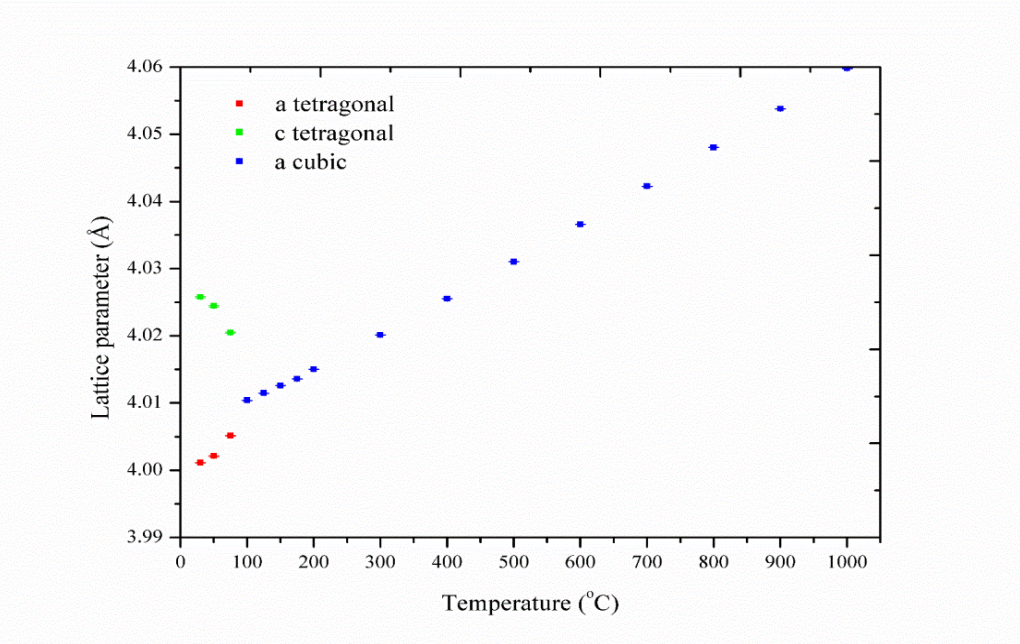

Figure 39. BGT0050 lattice parameters as a function of temperature with associated errors for each refined value.

Figures 40, 41 and 42 show the Rietveld refinement at 75°C (top) and 800°C (bottom) for BT0100, BGT0250 and BGT0500, respectively, and are representative of the goodness of fit. BGT0500 shows unusual peak broadening making it difficult to assign a proper space group. Cubic $Pm\bar{3}m$ space group was used for the samples BGT0100, BGT0250 and BGT0500 as there is no significant evidence for tetragonal to cubic phase transition; that is, there isn't discernible peak splitting or change in peak intensities. These materials reside in pseudo-cubic symmetry within the detection capability of the instrument.

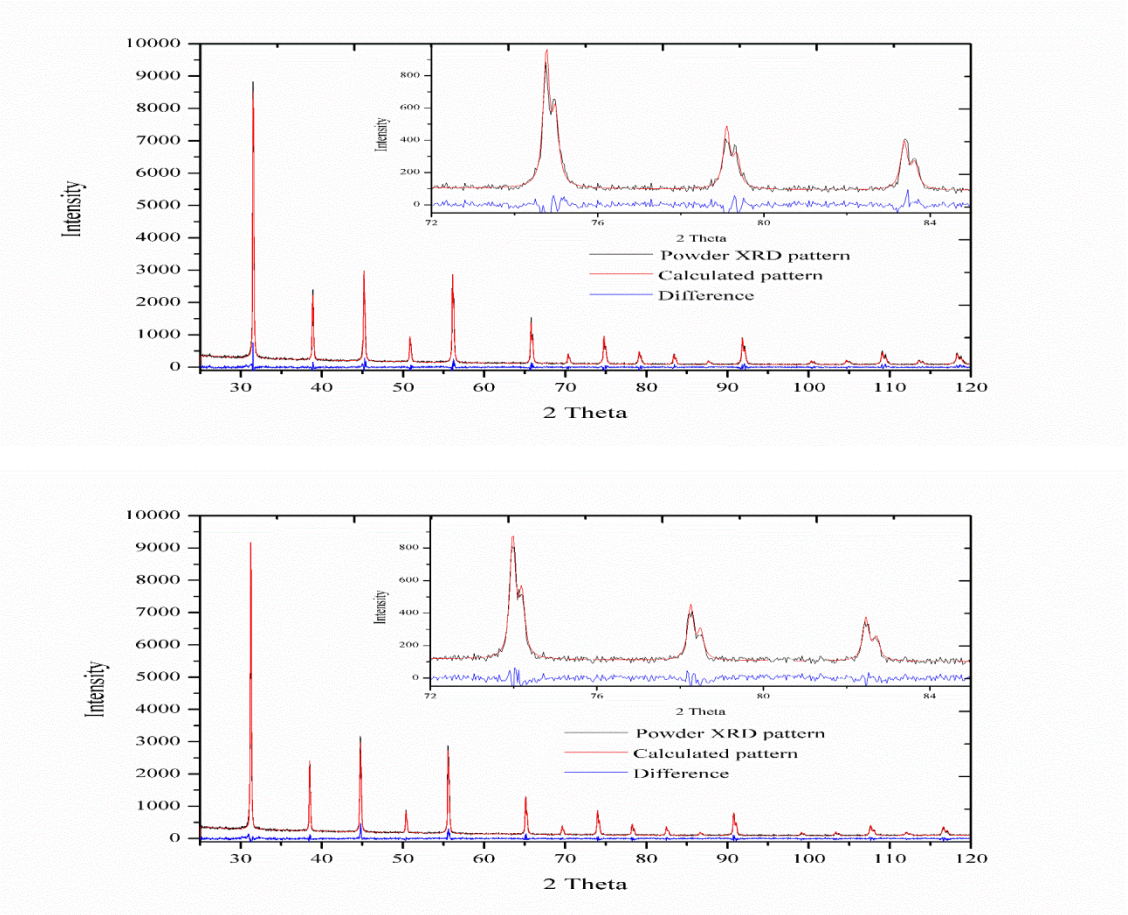

Figure 40. Rietveld refinement of BGT0100 at 75℃ (top) and 800℃ (bottom) illustrating the goodness of fit to the data.

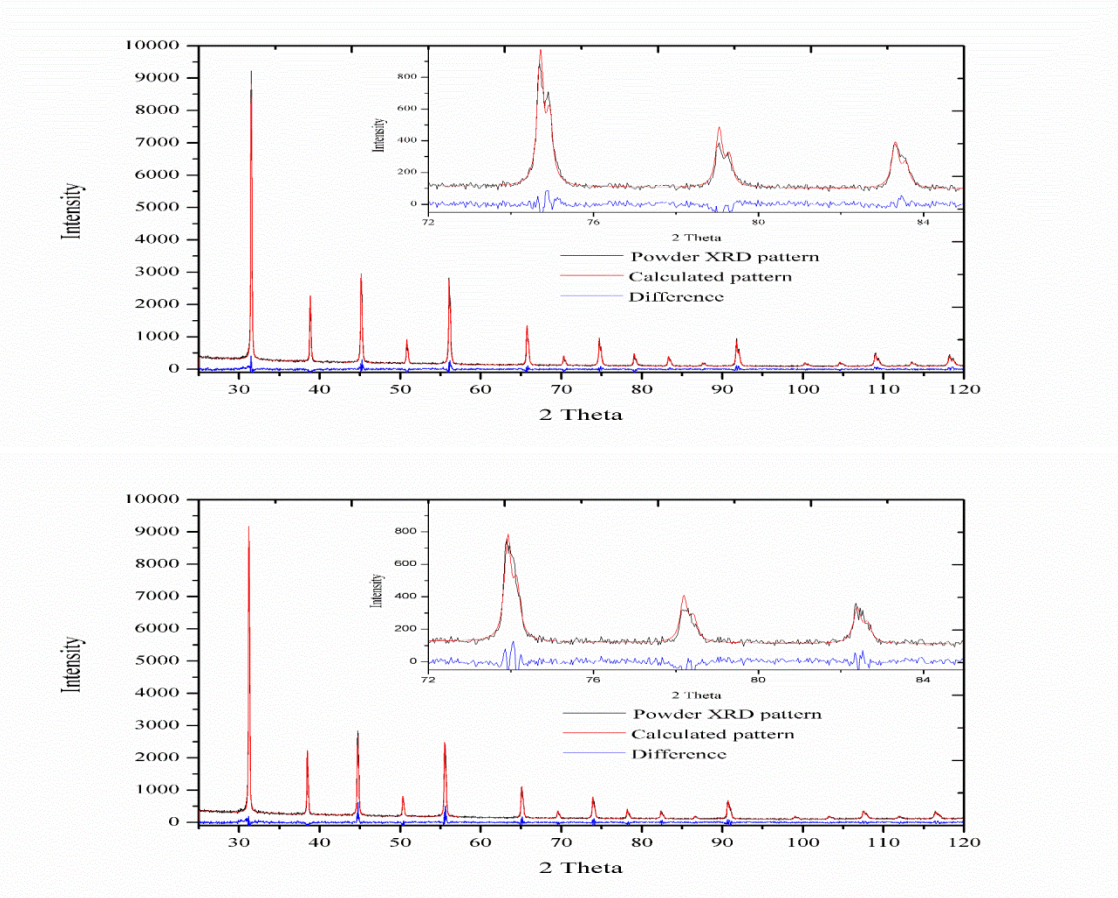

Figure 41. Rietveld refinement of BGT0250 at 75℃ (top) and 800℃ (bottom) illustrating the goodness of fit to the data.

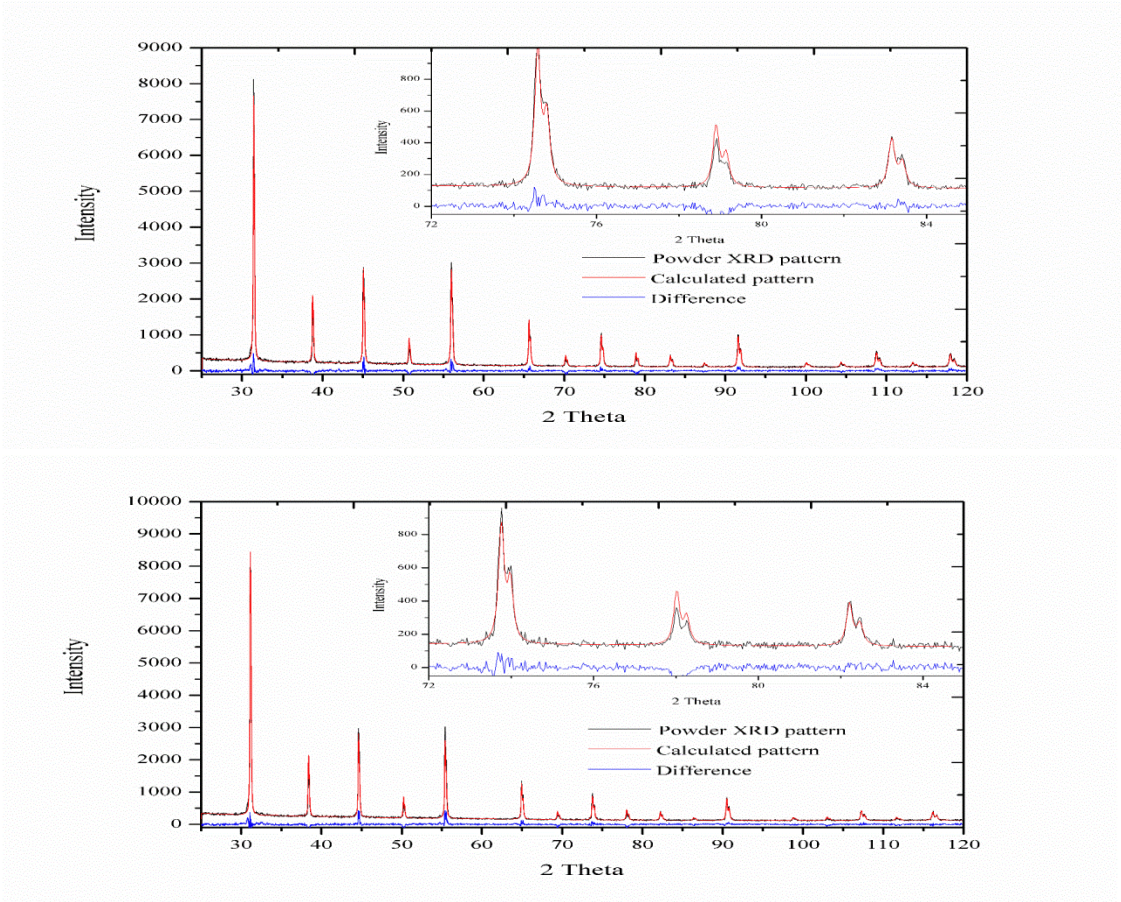

Figure 42. Rietveld refinement of BGT0500 at 75℃ (top) and 800°C (bottom) illustrating the goodness of fit to the data.

Figures 43, 44 and 45 show the lattice parameter with the associated error bars as a function of temperature for each refined value of BGT0100, BGT0250 and BGT0500, respectively. From the figure, there are two linear trend lines in the slope of each material and indicates a change in thermal expansion of the material. Note that a change in thermal expansion is usually an indication of a phase transformation. The points at which the thermal expansion changes occur for BGT0100 and BGT0250 are 150°C and 160°C, respectively, and these temperatures roughly coincide with changes in the slope of the resistivity of these same materials, respectively, as discussed within the electrical measurements section of this thesis. Interestingly, these temperatures do not correspond to the T_{max} in the ε_r response, which is very unusual for this class of materials including the well behaved ferroelectric materials. Further investigation into the local structure is needed to clarify the unusual behavior of these materials, BGT*x*, especially about the

demarcation point, between ferroelectric and DPT behavior, roughly x = 0.010. It is interesting to note that the degree of slope change in the lattice parameter vs temperature plot decreases with the increase in DP concentration and that the degree of tetragonality of BGTx decreases linearly with increasing DP concentration as shown in Figure 46. Figure 47 shows the lattice volume expansion as a function of temperature for BT, BGT0025, BGT0050, BGT0100, BGT0250 and BGT0500. The volume expansion is unusually high and cannot be explained through discussion of a hard sphere ionic radii model. For instance, using the room temperature six-fold coordinated ionic radii of Shannon Ga^{3+} (0.76 Å) and Ta^{5+} (0.78 Å) replacing Ti^{4+} (0.745 Å) the lattice parameter increases by about 0.0003, 0.0005, 0.0010, 0.0025 and 0.0050 Å for BGT0025, BGT0050, BGT0100, BGT0250 and BGT0500, respectively, which is significantly smaller than the experimental increases of 0.0017, 0.0024, 0.004, 0.006 and 0.011, respectively, by a factor of about 6, 5, 4, 3, and 2, respectively. However, the unusual volume expansion can be explained in terms of the internal electric field induced by the DP coupling. The induced internal electric field is the overall electric field resulting from superimposed long range electric field of the ferroelectric with the randomly dispersed DP induced electric field, which in general opposes the long range electric field, and results in the expansion of the effective ionic radii through an energy accounting process.

The C-T phase transition temperature *a priori* predicted by NSMM for BGT0500 was ~ 200 °C. Assuming a linear relationship of T_c, Vegard's Law, with the dipole substitutions, the extrapolated T_c values predicted by NSMM of 150°C and 170°C for BGT0100 and BGT0250 interestingly coincide with the observations from HTXRD and the resistivity measurements. While T_c for BGT0500 is difficulty to define since the slope change in the lattice parameter vs temperature plot does not extrapolate well due to uncertainty of associated errors, as shown in Figure 45, the crossing point in the figure is between 200 and 250°C and also is in reasonable agreement with the a priori prediction of ~ 200°C of NSMM.

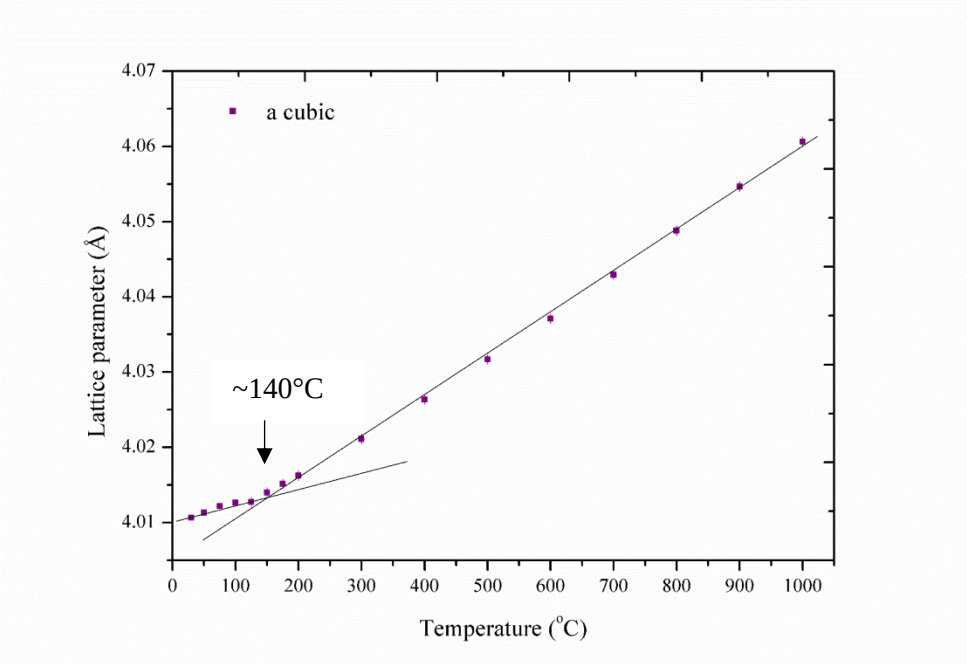

Figure 43. BGT0100 lattice parameter as a function of temperature with associated error bars.

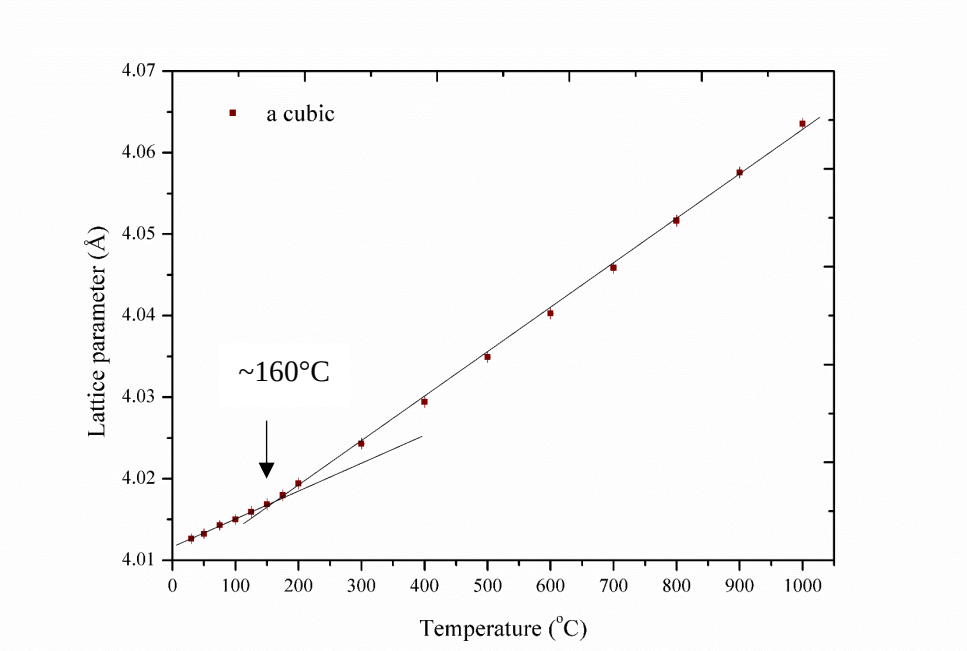

Figure 44. BGT0250 lattice parameter as a function of temperature with associated error bars.

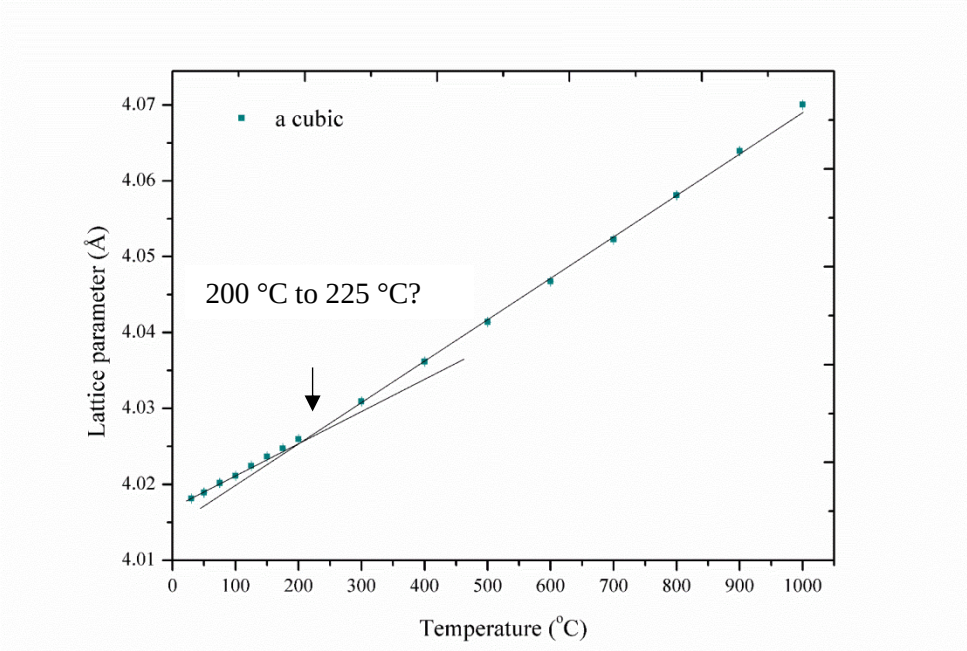

Figure 45. BGT0500 lattice parameter as a function of temperature with associated error bars.

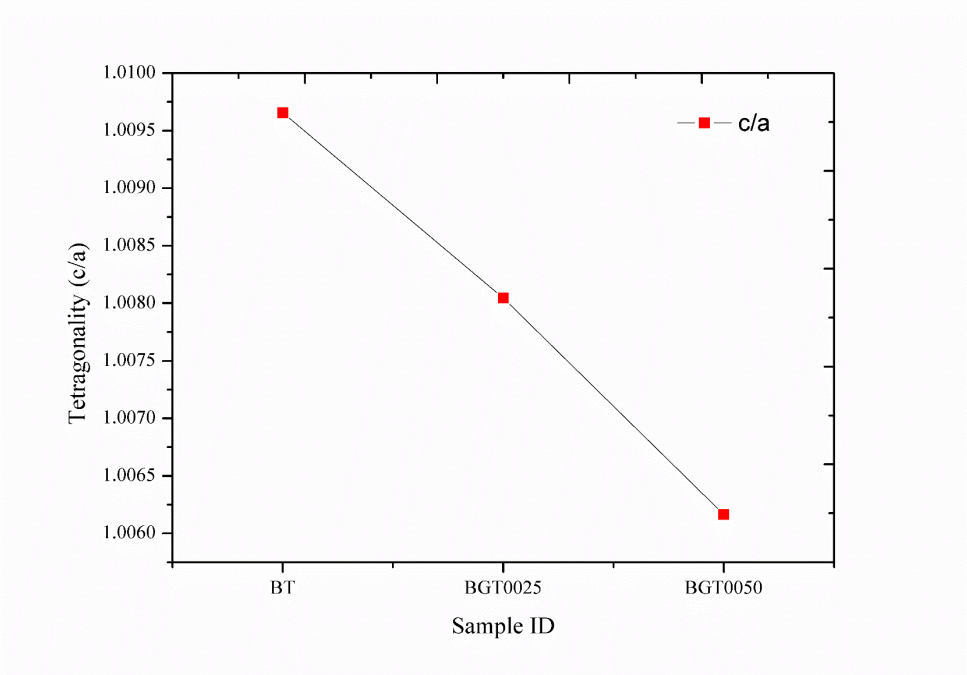

Figure 46. Material tetragonality as the function of DP concentration.

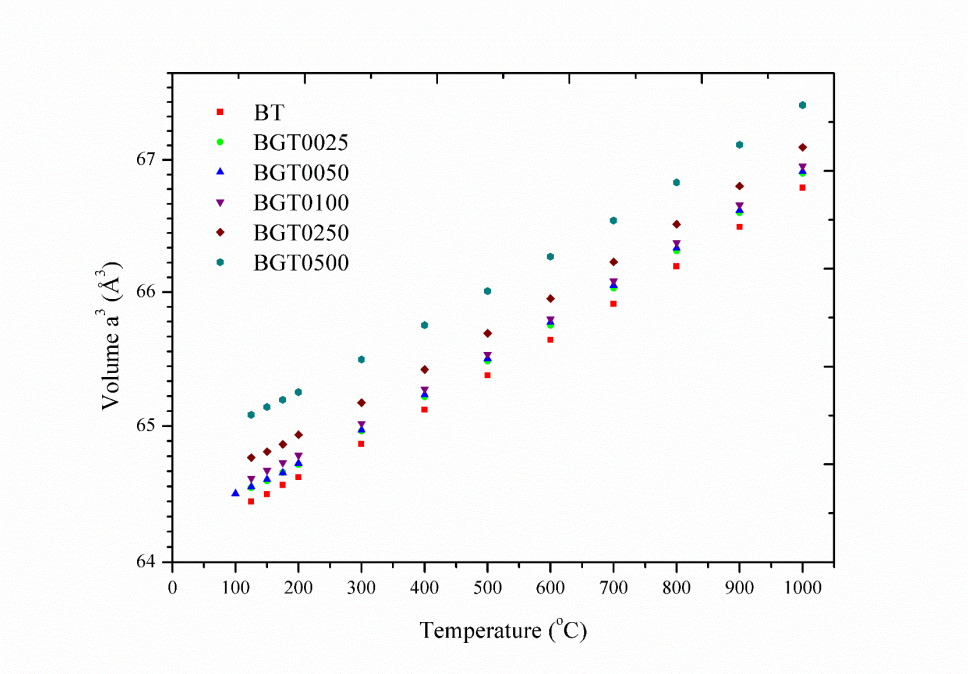

Figure 47. Lattice volume expansion as a function of temperature for BT, BGT0025, BGT0050, BGT0100, BGT0250 and BGT0500.

Table IX summarizes the crystal symmetry at RT, experimental unit cell dimensions at RT and the calculated thermal expansion coefficient for the temperature range [200 °C, 1000 °C] of BT, BGT0025, BGT0050, BGT0100, BGT0250 and BGT0500.

Table IX. Crystal Symmetry at RT, Experimental Unit Cell dimensions at RT and Thermal Expansion Coefficient of BT, BGT0025, BGT0050, BGT0100, BGT0250 and BGT0500

Sample ID	Crystal symmetry at RT	Lattice parameters at RT (Å)		Coefficient of thermal expansion X 10^{-6} (K^{-1})
		a	*c*	
BT	Tetragonal	3.994	4.033	13.69
BGT0025	Tetragonal	3.998	4.030	13.68
BGT0050	Tetragonal	4.001	4.026	13.71
BGT0100	Pseudo-cubic	4.011	N/A	13.57
BGT0250	Pseudo-cubic	4.013	N/A	13.52
BGT0500	Pseudo-cubic	4.018	N/A	13.41

SUMMARY AND CONCLUSION

In this work, fabrication of solid solution $Ba\{[Ga_x,Ta_x]Ti_{(1-2x)}\}O_3$ with x equal to 0, 0.0025, 0.005, 0.01, 0.025 and 0.05 has been successfully demonstrated using the solid-state reaction method. Ultra-high purity BT with a T_c of 131°C is reported in this work. The fabricated samples have been electrically and structurally characterized to understand the dielectric relaxation and DPT behavior. X-ray diffraction, ε_r, and resistivity have been examined for the BT, BGT0025, BGT0050, BGT0100, BGT0250 and BGT0500 samples. The work successfully demonstrates evolution of BT based materials from a well behaved ferroelectric material to materials with diffuse phase transitions and finally to relaxor-like behavior.

Dielectric response has been discussed in detail to explain the shift in Curie temperature as a function of dopant concentration. Data were fit with available and widely used models to discuss the degree of relaxation or diffuseness and to calculate the Curie constant and other related properties. The dielectric relaxation was discussed in terms of local electric fields induced by the DP's which act to reduce the co-operative ferroelectric long-range electric field within the parent matrix. The results were compared against well-behaved ferroelectric BT. The evolution of BT based ferroelectric materials to DPT materials helped to clearly differentiate the DPT in materials from relaxor behavior. DPT in materials may be due to quenched random electric field interactions in the parent material matrix which act to reduce the electric field while relaxor behavior is believed to result from compositional disorder in the A and/or B site in the perovskite structure that interrupts the long-range ferroelectric order. BGT0050 and BGT0100 show a diffuseness value as large as the widely studied lead based relaxor PMN-PT of 1.8. It is also interesting to state again that the Tetragonal-Orthorhombic phase transition was stabilized in BT, BGT0025 and BGT0050 whereas Cubic-Tetragonal phase transitions were lowered as the DP concentration increased.

DP substituted BT materials were compared against pure BT for electrical resistivity, RC time constant and activation energy. DP substituted BT shows enhanced resistivity and time constant at RT and above. The materials clearly fall into two separate

categories. The materials with low DP concentration BGT0025 and BGT0050, show a lower resistivity, which might be the intrinsic effect of dopants and acceptors separated in the parent matrix and without significant local electric field from DP couplies. At high enough concentration, the probability of donor and acceptor coupling statistically increases being increased, and results in enhanced resistivity because of the local field interaction. Increased resistivity combined with high ε_r at and near RT results in increased RC time constant, which should be of interest for some specific applications.

High temperature X-ray diffraction was used to calculate the lattice parameters, volume expansion, thermal expansion coefficients and the Curie temperature of each material. Materials were also discussed in two categories. The first category low DP concentration materials, BGT0025 and BGT0050, show a ferroelectric behavior and the Curie temperatures were calculated using Rietveld refinement results and compared with dielectric measurements. The calculated values are in good agreement with the electrical measurements.

The second category, BGT0100, BGT0250 and BGT0500, show a pseudo-cubic symmetry within the measurement capability of the instrument. The tetragonality has been shown to reduce with an increase in DP concentration and a volume expansion has been observed as a function of DP concentration. The volume expansion may be associated with the effective ionic radii increase which react to minimize the energy due to the local field interaction induced by the DP's.

Table X summarizes the T_c predicted by NSMM and observed in ε_r response, resistivity measurements and HTXRD measurements for each of the composition.

Table X. Curie Temperature predicted by NSMM and observed in ε_r response, Resistivity measurements and HTXRD measurements for each of the composition

Sample ID	NSMM	T_c from ε_r response (°C)	T_c from ρ measurements (°C)	T_c from *HTXRD* measurements (°C)
BT	130	131	~120	125
BGT0025	141	112	~100	100-125
BGT0050	154	91	~85	75-100
BGT0100	~167	~130	160	~140
BGT0250	~180	~135	140	~160
BGT0500	~200	N/A	135	~200-225

FUTURE WORK

Although there have been many research efforts with regard to various lead based and lead free ferroelectric and relaxor ferroelectric materials, the complete understanding of perovskite based ferroelectric materials is still incomplete. Since electrical behavior of materials especially ferroelectricity is a co-operative phenomenon, it is challenging to develop a model that can be used to predict electrical properties of materials, taking into consideration all the local and long range electric field interactions. Predicting electrical properties, crystal structures and related material properties is desired to support society by reducing the human effort and saving time and resources.

This work serves as a small step towards developing a complete material model that can predict the electrical properties of ferroelectric perovskite based materials. This work examines a proposed model for its applicability in complex perovskite material systems and explains the various exhibited material properties. The unusual material properties of DP-(Ga,Ta) substituted BT were explained in conjecture with dipole-like interactions of the dopant and acceptor separated by a distance in the parent material matrix. Since this DP will induce both local disorder and long range order, it is very important to understand the local structure of these relaxor-like materials to completely understand the material behavior.

Local structural investigations were not done within this. This thesis mainly focused on documenting the feasibility of fabricating perovskite based solid solutions with both donors and acceptors substituted in the structure, to investigate the solubility limit and to explain the electrical/ dielectric and resistivity measurements. In the future, investigations on local distributions of donors and acceptors and their local and long-range interactions would be of interest to better understand the material. Performing temperature dependent spectroscopic techniques like Raman spectroscopy would be helpful to better understand the structural characteristics of these material. Since there are reports of these materials exhibiting competitive electric field tunability, further investigating electric field tunable capabilities can be of interest for some material applications.

The increased resistivity and increased time constants, diffuseness of the ε_r, peak value of ε_r, and phase transition temperature of BT matrix material as a function of DP substitution. The dielectric properties, through systematic introduction of DPs in the BT matrix, yield materials that should be of significant interest for a wide range of electro-ceramic devices. Through continued systematic control of DP concentrations, the material properties can be further optimized for the specific dielectric device In addition, dielectric breakdown strengths of these materials can be useful in understanding the effect the DP has on the band structure as well as for determining potential use for energy storage.

REFERENCES

1. J. P. Attfield, P. Lightfoot, and R. E. Morris, "Perovskites," *Dalton Trans.,* **44** [23] 10541-2 (2015)

2. M. Yashima and R. Ali, "Structural Phase Transition and Octahedral Tilting in the Calcium Titanate Perovskite $CaTiO_3$," *Solid State Ionics,* **180** [2] 120-6 (2009).

3. A. Bhalla, R. Guo, and R. Roy, "The Perovskite Structure–a Review of Its Role in Ceramic Science and Technology," *Mater. Res. Innovations,* **4** [1] 3-26 (2000).

4. A. Glazer, "Simple Ways of Determining Perovskite Structures," *Acta Crystallogr., Sect. A: Cryst. Phys., Diffr., Theor. Gen. Crystallogr.,* **31** [6] 756-62 (1975).

5. C. J. Howard, B. J. Kennedy, and P. M. Woodward, "Ordered Double Perovskites–a Group-Theoretical Analysis," *Acta Crystallogr., Sect. B: Struct. Sci.,* **59** [4] 463-71 (2003).

6. R. J. Tilley, *Perovskites: Structure-Property Relationships, 1st ed.;* pp. 341-343. John Wiley & Sons, Chichester, West Sussex, PO19 8SQ, UK, 2016.

7. G. H. Haertling, "Ferroelectric Ceramics: History and Technology," *J. Am. Ceram. Soc.,* **82** [4] 797-818 (1999).

8. P. K. Panda and B. Sahoo, "PZT to Lead Free Piezo Ceramics: A Review," *Ferroelectrics,* **474** [1] 128-43 (2015).

9. V. V. Mitic, Z. S. Nikolic, V. B. Pavlovic, V. Paunovic, M. Miljkovic, B. Jordovic, and L. Zivkovic, "Influence of Rare-Earth Dopants on Barium Titanate Ceramics Microstructure and Corresponding Electrical Properties," *J. Am. Ceram. Soc.,* **93** [1] 132-7 (2010).

10. L. A. Xue, Y. Chen, and R. J. Brook, "The Influence of Ionic Radii on the Incorporation of Trivalent Dopants into $BaTiO_3$," *Mater. Sci. Eng.: B,* **1** [2] 193-201 (1988).

11. D. Jablonskas, R. Grigalaitis, J. Banys, A. Bokov, and Z.-G. Ye, "Broadband Dielectric Spectra in $PbMg_{1/3}Nb_{2/3}O_3$ Crystals with Chemical Order Modified by La Doping," *Appl. Phys. Lett.,* **107** [14] 142905 (2015).

12. G. Trolliard and V. Dorcet, "Reinvestigation of Phase Transitions in $Na_{0.5}Bi_{0.5}TiO_3$ by TEM Part II: Second Order Orthorhombic to Tetragonal Phase Transition," *Chem. Mater.,* **20** [15] 5074-82 (2008).

13. W. Zhong and D. Vanderbilt, "Competing Structural Instabilities in Cubic Perovskites," *Phys. Rev. Lett.,* **74** [13] 2587 (1995).

14. V. M. Goldschmidt, "Die Gesetze Der Krystallochemie," *Nature,* **14** [21] 477-85 (1926).

15. G. Beskow, "V. M Goldschmidt: Geochemische Verteilungsgesetze Der Elemente," *Geol. Assoc. Stockholm Negotiations,* **46** [6-7] 738-43 (1924).

16. R. D. Shannon, "Revised Effective Ionic Radii and Systematic Studies of Interatomic Distances in Halides and Chalcogenides," *Acta Crystallogr., Sect. A: Cryst. Phys., Diffr., Theor. Gen. Crystallogr.,* **32** [5] 751-67 (1976).

17. V. Miller and S. Tidrow, "Review: New Simple Material Model Versus Goldschmidt's Tolerance Factor Formalism," *Ferroelectrics,* **503** [1] 149-62 (2016).

18. S. C. Tidrow, "Mapping Comparison of Goldschmidt's Tolerance Factor with Perovskite Structural Conditions," *Ferroelectrics,* **470** [1] 13-27 (2014).

19. S. C. Tidrow, "Linking Curie Constant and Phase Transition Temperature with Fundamental Ion Properties," *Integr. Ferroelectr.,* **174** [1] 15-25 (2016).

20. A. J. Moulson and J. M. Herbert, *Electroceramics: Materials, Properties, Applications, 2nd ed.;* pp. 20-60. John Wiley & Sons, 2003.

21. H. Neugebauer, "Clausius-Mosotti Equation for Certain Types of Anisotropic Crystals," *Can. J. Phys.,* **32** [1] 1-8 (1954).

22. R. D. Shannon, "Dielectric Polarizabilities of Ions in Oxides and Fluorides," *J. Appl. Phys.,* **73** [1] 348-66 (1993).

23. T. Dakin, "Conduction and Polarization Mechanisms and Trends in Dielectric," *IEEE Electr. Insul. Conf.,* **22** [5] 11-28 (2006).

24. R. Alias, "Structural and Dielectric Properties of Glass-Ceramic Substrate with Varied Sintering Temperatures," pp. 89-118 in Sintering Applications Handbook, Edited by Burcu Ertug, INTECH Open Access Publisher, Croatia, 2013.

25. C. Randall, R. Newnham, and L. Cross, "History of the First Ferroelectric Oxide, $BaTiO_3$," *Materials Research Institute, The Pennsylvania State University, University Park, Pa, USA,* (2004).

26. K. Uchino, "Glory of Piezoelectric Perovskites," *Sci. Technol. Adv. Mater.,* **16** [4] 1-16 (2015).

27. G. Robert. "Transducer and method of making the same," U.S. Pat. 2,486,560, November-1949.

28. A. Von Hippel, "Ferroelectricity, Domain Structure, and Phase Transitions of Barium Titanate," *Rev. Mod. Phys.,* **22** [3] 221 (1950).

29. H. D. Megaw, "Crystal Structure of Barium Titanate," *Nature,* **155** [3938] 484-5 (1945).

30. H. F. Kay and P. Vousden, "Xcv. Symmetry Changes in Barium Titanate at Low Temperatures and Their Relation to Its Ferroelectric Properties," *The London, Edinburgh, and Dublin Philos. Mag. J. Sci.,* **40** [309] 1019-40 (1949).

31. E. Aksel and J. L. Jones, "Advances in Lead-Free Piezoelectric Materials for Sensors and Actuators," *ACS Sens.,* **10** [3] 1935-54 (2010).

32. G. L. Wynick, "The Effect of Lattice Protons on the Raman Activity of $BaTiO_3$ Utilizing High-Temperature Micro Raman Spectroscopy," Master of Science Thesis. Alfred University, Alfred, NY, 2010.

33. M. Garrett, J. Chang, H. Jenssen, and C. Warde, "A Method for Poling Barium Titanate, $BaTiO_3$," *Ferroelectrics,* **120** [1] 167-73 (1991).

34. R. J. Tilley, *Understanding Solids: The Science of Materials, 2nd ed.;* pp. 341-343. John Wiley & Sons, Chichester, West Sussex, PO19 8SQ, UK, 2004.

35. D. Viehland, S. Jang, L. E. Cross, and M. Wuttig, "Deviation from Curie-Weiss Behavior in Relaxor Ferroelectrics," *Phys. Rev. B,* **46** [13] 8003 (1992).

36. A. Bokov and Z. G. Ye, "Recent Progress in Relaxor Ferroelectrics with Perovskite Structure," *Ferroelectrics,* **31** (2006).

37. L. E. Cross, "Relaxor Ferroelectrics," *Ferroelectrics,* **76** [1] 241-67 (1987).

38. M. Lente, E. Moreira, D. Garcia, J. Eiras, P. Neves, A. Doriguetto, V. Mastelaro, L. Lopes, and Y. Mascarenhas, "Crossover from Ordinary Ferroelectric to Relaxor State: A Pre-Transitional Martensitic Transformation," *Ferroelectrics,* **339** [1] 121-8 (2006).

39. R. Moreira and R. Lobo, "Phenomenological Study of Diffuse Phase Transitions," *J. Phys. Soc. Jpn.,* **61** [6] (1992).

40. C. Randall, D. Barber, R. Whatmore, and P. Groves, "A Tem Study of Ordering in the Perovskite, $Pb(Sc_{1/2}Ta_{1/2})O_3$," *J. Mater. Sci.,* **21** [12] 4456-62 (1986).

41. S. M. Pilgrim, A. E. Sutherland, and S. R. Winzer, "Diffuseness as a Useful Parameter for Relaxor Ceramics," *J. Am. Ceram. Soc.,* **73** [10] 3122-5 (1990).

42. A. Tombak, J.-P. Maria, F. Ayguavives, Z. Jin, G. T. Stauf, A. I. Kingon, and A. Mortazawi, "Tunable Barium Strontium Titanate Thin Film Capacitors for RF and Microwave Applications," *IEEE Microwave and Wireless Compon. Lett.,* **12** [1] 3-5 (2002).

43. X. Chou, J. Zhai, H. Jiang, and X. Yao, "Dielectric Properties and Relaxor Behavior of Rare-Earth (La, Sm, Eu, Dy, Y) Substituted Barium Zirconium Titanate Ceramics," *J. Appl. Phys.,* **102** [8] 084106 (2007).

44. A. Zeb and S. J. Milne, " Stability of High-Temperature Dielectric Properties for $(1-X)Ba_{0.8}Ca_{0.2}TiO_3–XBi(Mg_{0.5}Ti_{0.5})O_3$ Ceramics," *J. Am. Ceram. Soc.,* **96** [9] 2887-92 (2013).

45. S. U. Jan, A. Zeb, and S. J. Milne, "Dielectric Ceramic with Stable Relative Permittivity and Low Loss from −60 to 300°C: A Potential High Temperature Capacitor Material," *J. Eur. Ceram. Soc.,* **36** [11] 2713-8 (2016).

46. H. Martirena and J. Burfoot, "Grain-Size Effects on Properties of Some Ferroelectric Ceramics," *J. Phys. C: Solid State Phys.,* **7** [17] 3182 (1974).

47. D. F. Hennings, B. S. Schreinemacher, and H. Schreinemacher, "Solid-State Preparation of $BaTiO_3$-Based Dielectrics, Using Ultrafine Raw Materials," *J. Am. Ceram. Soc.,* **84** [12] 2777-82 (2001).

48. F. J. Crowne, S. C. Tidrow, D. M. Potrepka, and A. Tauber, "Microfields Induced by Random Compensated Charge Pairs in Ferroelectric Materials," *Cambridge Univ. Press,* **720** H5-1 (2002).

49. A. Feteira, D. C. Sinclair, I. M. Reaney, Y. Somiya, and M. T. Lanagan, "$BaTiO_3$-Based Ceramics for Tunable Microwave Applications," *J. Am. Ceram. Soc.,* **87** [6] 1082-7 (2004).

50. T. R. Mion, D. M. Potrepka, F. J. Crowne, A. Tauber, and S. C. Tidrow, "Electrical and Structural Properties of $Ba(Y^{3+},Sb^{5+})_{0.05}Ti_{0.90}O_3$," *Integr. Ferroelectr.,* **148** [1] 17-26 (2013).

51. D. Rase and R. Roy, "Phase Equilibria in the System $BaO–TiO_2$," *J. Am. Ceram. Soc.,* **38** [3] 102-13 (1955).

52. Hewlett Packard, 4284A Precision LCR Meter Operational Manual. Hewlett Packard, Japan, 1998.

53. J. Ravez and A. Simon, "Temperature and Frequency Dielectric Response of Ferroelectric Ceramics with Composition $Ba(Ti_{1-x}Zr_x)O_3$," *Eur. J. Solid State Inorg. Chem.,* **34** [11] 1199-209 (1997).

54. T. Mion, D. M. Potrepka, F. J. Crowne, A. Tauber, and S. C. Tidrow, "Dielectric and X-Ray Diffraction Analysis of $Ba(Ga,Ta)_{0.05}Ti_{0.90}O_3$," *Ferroelectrics,* **473** [1] 13-23 (2014).

55. A. A. Bokov and Z. G. Ye, "Dielectric Relaxation in Relaxor Ferroelectrics," *J. Adv. Dielectr.,* **2** [02] 1241010 (2012).

56. A. Feteira, D. C. Sinclair, I. M. Reaney, and M. T. Lanagan, "Structure–Property Relationships of $BaTi_{1-2y}Ga_yNb_yO_3$ ($0 \leq Y \leq 0.35$) Ceramics," *J. Am. Ceram. Soc.*, **88** [11] 3055-62 (2005).

57. S. Lokare, "Structural and Electrical Properties of $BaTiO_3$ Prepared by Solid State Route," *Int. J. Chem. Phys. Sci.,* **4** 154-161 (2005)

58. L. Srisombat, S. Ananta, B. Singhana, T. R. Lee, and R. Yimnirun, "Chemical Investigation of Fe^{3+}/Nb^{5+}-Doped Barium Titanate Ceramics," *Ceram. Int.,* **39** S591-S594 (2013).

59. C. Miot, E. Husson, C. Proust, R. Erre, and J. Coutures, "X-Ray Photoelectron Spectroscopy Characterization of Barium Titanate Ceramics Prepared by the Citric Route. Residual Carbon Study," *J. Mater. Res.,* **12** [09] 2388-92 (1997).

60. S. M. Mukhopadhyay and T. C. Chen, "Surface Chemical States of Barium Titanate: Influence of Sample Processing," *J. Mater. Res.,* **10** [06] 1502-7 (1995).

61. Z. Yao, H. Liu, Y. Liu, Z. Wu, Z. Shen, Y. Liu, and M. Cao, "Structure and Dielectric Behavior of Nd-Doped $BaTiO_3$ Perovskites," *Mater. Chem. Phys.,* **109** [2] 475-81 (2008).

62. S. A. Nasser, "X-Ray Photoelectron Spectroscopy Study on the Composition and Structure of $BaTiO_3$ Thin Films Deposited on Silicon," *Appl. Surf. Sci.,* **157** [1] 14-22 (2000).

63. B. Vugmeister and M. Glinchuk, "Dipole Glass and Ferroelectricity in Random-Site Electric Dipole Systems," *Rev. Mod. Phys.,* **62** [4] 993 (1990).